MICROFAUNAL RECORDING OF RECENT ENVIRONMENTAL CHANGES IN THE HERSCHEL BASIN, WESTERN ARCTIC OCEAN

Jade Falardeau[1],*, Anne de Vernal[1], Marit-Solveig Seidenkrantz[2], Thomas M. Cronin[3], Laura Gemery[3], Léo Chassiot[4], Michael Fritz[5], Vladislav Carnero-Bravo[1,6], Claude Hillaire-Marcel[1] and Philippe Archambault[7]

ABSTRACT

Microfaunal assemblages of benthic foraminifera, ostracods, and tintinnids from two marine sediment cores retrieved from the Herschel Basin of the Canadian Beaufort Sea shelf document relationships with environmental parameters such as salinity, sea-ice cover, and turbulence. Cores YC18-HB-GC01 and PG2303-1 were collected at 18 and 32 m water depth, respectively. At these sites, sediment accumulation rates range between 0.6 and 1.7 cm yr^{-1} allowing a near-annual temporal resolution over the last 50 years. Multivariate analyses indicate that benthic foraminiferal assemblages respond primarily to food supply. Dissimilarities between the microfaunal assemblages of the two cores are mainly the result of bottom water salinity levels linked to water depth. High abundance of the benthic foraminiferal species *Elphidium clavatum* and occurrences of *Elphidium bartletti* point to varying, but relatively low, salinities at the shallow core site YC18-HB-GC01, which may be affected by variations in the summer halocline depth. Higher species diversity and more abundant *Cassidulina reniforme* and *Stainforthia feylingi* characterize the deeper core PG2303-1, which might reflect more stable conditions and higher bottom-water salinities throughout the studied time interval. The most important microfaunal shift of the last 50 years, observed in the shallower longer core YC18-HB-GC01, occurred at the turn of the 21st century. Prior to ~2000 CE, the presence of *Islandiella norcrossi* indicates more stable and saline conditions. Since ~2000 CE, increased abundances of *Haynesina nivea* and of the ciliate *Tintinnopsis fimbriata* suggest decreased salinity and increased turbidity. An increased abundance of *Eoeponidella pulchella* after ~2000 CE suggests a concurrent increase in productivity in the last two decades. This shift is nearly synchronous with a decrease in mean summer sea-ice concentration, which can play an important role in bottom water stability on the shelf. Easterly winds can induce a reduction in the sea-ice cover, but also foster a westward spreading of the Mackenzie River plume and the upwelling of nutrient-rich Pacific waters onto the shelf. Both factors would explain the increased freshening and productivity of the Herschel Basin. The last two decades were also marked by a decrease in ostracod abundance that may relate to higher water turbidity. This study shows that combining information from benthic foraminifera, ostracods, and tintinnids provides a comprehensive insight into recent hydrographic/climatic changes in nearshore Arctic habitats, where productivity is critical for the food security of local communities.

INTRODUCTION

The 21st century marks the lowest level of sea-ice extent in the Arctic Ocean of the last 1400 years (Kinnard et al., 2011; IPCC, 2019). This decrease has led to increased net primary production, essentially due to both a longer open water season and an increased area of open water (Arrigo et al., 2008; Barber et al., 2012; Arrigo & van Dijken, 2015), at least until ca. 2008 CE. However, since then, new nutrients imported to the Arctic Ocean from the Pacific and the Atlantic oceans have become a major contributor to the increase in net primary production (Lewis et al., 2020). Partial ice cover also fosters upwelling of nutrient-rich waters onto the Arctic shelves (Barber et al., 2012; Schulze & Pickart, 2012) that act as a hotspot for phytoplankton blooms (Tremblay et al., 2011, 2012; Walkusz et al., 2012). However, a transition to a seasonally ice-free Arctic Ocean raises questions about the long-term effects of changes in the plankton community (Li et al., 2009; Comeau et al., 2011; Dolan et al., 2014; Lefebvre et al., 2016) and the impact of the stratification and vertical mixing of the water masses (McLaughlin & Carmack, 2010; Blais et al., 2017) on the Arctic marine food web. Open waters also contribute to the exchange of heat with the atmosphere and to a generally more unstable climate due to increased wind speed and storm events (Simmonds & Keay, 2009; Mioduszewski et al., 2018). Along Arctic coastlines, higher air temperatures and reduced sea-ice cover enhance coastal erosion, which increases the flux of carbon and sediment to the continental shelves, also affecting the food web (Fritz et al., 2017). The role of terrigenous nutrients linked to coastal erosion is rarely considered (Ardyna & Arrigo, 2020; Lewis et al., 2020), but could contribute up to 21% of the primary production in the Arctic Ocean (Terhaar et al., 2021). However, coastal erosion also leads to increased turbidity in the nearshore areas (Klein et al., 2019, Jong et al., 2020), with a documented negative impact on primary production (Anthony et al., 2004; Retamal et al., 2008; Bonsell & Dunton, 2018; Lewis et al., 2020). It may also contribute to ocean acidification through the degradation of terrestrial organic matter (Semiletov et al., 2016; Fritz et al., 2017).

[1] Geotop Research Center in Earth System Dynamics and Département des sciences de la Terre et de l'atmosphère, Université du Québec à Montréal, Montréal, Canada

[2] Paleoceanography and Paleoclimate Group, Arctic Research Centre, and iClimate centre, Department of Geoscience, Aarhus University, Aarhus, Denmark

[3] U.S. Geological Survey, Florence Bascom Geoscience Center, National Center, Reston, VA, USA

[4] Département de Géographie, Faculté de foresterie, de géographie et de géomatique, Université Laval, Centre d'Étude Nordique and INRS-ETE, Québec, Canada

[5] Permafrost Research Unit, Alfred Wegener Institute, Helmholtz Centre for Polar and Marine Research, Potsdam, Germany

[6] Instituto de Ecología, Universidad del Mar, Campus Puerto Ángel, Puerto Ángel, Oaxaca, México

[7] Québec Océan, ArcticNet, Takuvik, Département de biologie, Université Laval, Québec, Canada

* Correspondence author. E-mail: falardeau.jade@courrier.uqam.ca

20

In coastal Arctic environments, it is often difficult to disentangle the impacts of the recent climate change from interannual and local variations because direct measurements over several decades are rare, especially when it comes to the biota. Micropaleontological tracers can be used to develop such biological time series and to reconstruct longer-term changes in environmental conditions. Among microfossils, benthic foraminiferal assemblages are largely controlled by water depth, salinity, temperature (e.g., Polyak et al., 2002, 2003), and food availability (carbon fluxes; e.g., Wollenburg & Kuhnt, 2000). Moreover, some species thrive in sea-ice marginal conditions (Scott et al., 2008a; Seidenkrantz, 2013; Seidenstein et al., 2018), while others may tolerate reduced dissolved oxygen availability (Seidenkrantz, 2013; Moffitt et al., 2014). In shallow benthic environments, ostracods are also abundant and represented by numerous species (Gemery et al., 2017). Their assemblages relate to salinity and temperature, sea level, and river inputs (McDougall et al., 1986; Reimnitz et al., 1993; Stepanova et al., 2003, 2007; Gemery et al., 2013, 2017, 2021; Cronin et al., 2017), in addition to sea-ice cover (Cronin et al., 2010). Tintinnid microfossils may also occur in marine sediment of the Arctic. They belong to ciliates, which are important grazers in the western Arctic Ocean microzooplankton community (Sherr et al., 2009). Previous studies of tintinnids have highlighted their potential use as tracers of salinity and sea level (Echols & Fowler, 1973; Burkovsky, 1976; Rogers et al., 1981; Pierce & Turner, 1993).

Several studies have documented the spatial distribution and ecological affinities of benthic foraminifera on Arctic continental shelves (e.g., Hald & Steinsund, 1996; Wollenburg & Mackensen, 1998; Wollenburg & Kuhnt, 2000; Polyak et al., 2002; Lloyd, 2006; Scott et al., 2008a, 2008b; Husum et al., 2015). However, high-resolution temporal reconstructions of past nearshore environments of the Arctic using benthic foraminifera are rare due to the lack of continuous sedimentological records. In this study, the Herschel Basin provides us with the opportunity to establish multi-annual time series (Grotheer et al., 2020) of microfaunal changes in a nearshore Arctic area that is presently influenced by sea-ice loss (Frey et al., 2015) and increased terrestrial supply from coastal erosion and rivers (Doxaran et al., 2015; Ehn et al., 2019; Klein et al., 2019; Jong et al., 2020). The Herschel Basin is located off northern Yukon, Canada (Fig. 1), where benthic foraminiferal and ostracod assemblages have not hitherto been documented. Thus, our first objective is to describe the microfaunal assemblages that characterize the last decades at two different depths in the basin, which may be used as a baseline for future paleo studies on the Beaufort Sea continental shelf. The second objective is to document interannual variations of the microfaunal records and eventually, to relate these to recent environmental changes and develop their use as tracers of biogenic productivity and diversity in nearshore Arctic areas.

REGIONAL SETTINGS

The Herschel Basin

The Herschel Basin is located on the continental shelf of the Beaufort Sea offshore the northern Yukon coastal plain,

around 10 km east of Herschel Island – Qikiqtaruk and 135 km west of Shallow Bay (Fig. 1B, D). This 40-km long, 15-km wide, and up to 70-m deep basin (EBA Engineering Consultants Ltd., 1992; Fig. 1D) allows continuous sediment accumulation (Grotheer et al., 2020). A shallow sill with a water depth of 13 m forms the northern limit of the basin (EBA Engineering Consultants Ltd., 1992). The sill prevents large stamukhi, or sea-ice rubble, and other floating ice from reaching the basin. The land-fast ice is generally 2 m thick on the shelf (Carmack & MacDonald, 2002), which also limits ice scouring at depth in the basin.

Hydrography

The regional hydrography of the Herschel Basin area is complex and unstable as it is controlled by winds that vary in direction and strength (see below; Kulikov et al., 1998; Lin et al., 2020). In summer, the predominantly eastward coastal flow (Fig. 1B, purple) carries relatively warm and low salinity waters alongshore (>0°C and <31 psu, respectively) that derive from the Bering summer waters (Lin et al., 2020). The shelf current (Fig. 1B, green arrow) flows predominantly westward and carries cold (<–1°C) and relatively fresh (<31 psu) surface waters (<30 m) mainly formed from sea-ice melt and meteoric waters (Kulikov et al., 1998; Weingartner et al., 2017; Lin et al., 2020). In contrast, at the shelf break, the waters flow eastward as the "Beaufort shelfbreak jet" (Fig. 1A, B, blue arrow) transporting predominantly the relatively saline (>31.5 psu) and nitrate-rich Pacific winter water mass known as the remnant winter waters (hereafter referred to as Pacific waters; Pickart, 2004; Lin et al., 2016, 2020). These waters sit on top of dense and saline subsurface Atlantic waters (>33.5 psu; Lin et al., 2016, 2020; Ardyna et al., 2017; Fig. 1C). Further to the north, the Beaufort Gyre circulates clockwise (Fig. 1A, B, yellow arrow) under the influence of the Beaufort Sea High (Serreze & Barrett, 2011). Part of the southern gyre recirculates into the Mackenzie Trough (Lin et al., 2020; Fig. 1B, thin yellow arrows). A strong anticyclonic regime generates dominant easterly winds in the marginal seas that induce sea-ice drift to the central Arctic Ocean usually resulting in reduced sea-ice cover (Ogi & Wallace, 2007; Ogi et al., 2008). Increased easterly winds in the Beaufort Sea continental slope area under a strong Beaufort Sea High would also reduce the entry of Pacific waters through the Beaufort shelfbreak jet (Brugler et al., 2014).

The Mackenzie River is the most important freshwater source in the area (Carmack et al., 2006), and it has the fourth largest discharge of freshwater into the Arctic Ocean (Holmes et al., 2011). Its main freshwater flux usually occurs at the beginning of June during the spring freshet (Carmack & MacDonald, 2002). The Mackenzie River plume is very rich in dissolved organic carbon (Holmes et al., 2011; Juhls, 2021) and terrestrial suspended particles (Doxaran et al., 2015), both of which are dispersed up to hundreds of kilometers westward during the freshet and depending on the winds during summer (Wood et al., 2015; Juhls, 2021). The Firth and Babbage estuaries are located approximately 20 km and 40 km, respectively, from our study site (Fig. 1B). However, their impact on the hydrography of the study area is low as their mean summer flow is significantly less than that
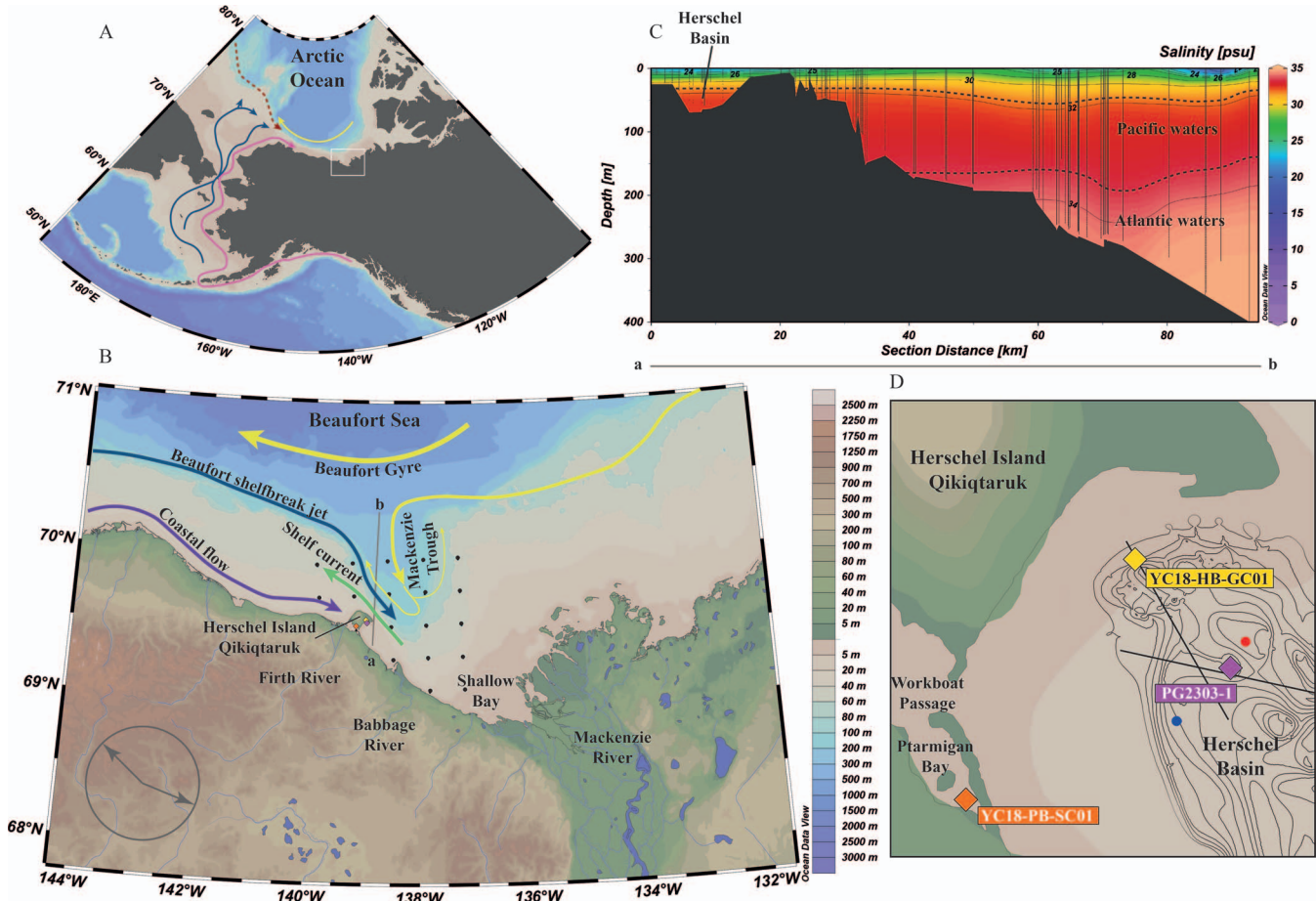
FIGURE 1. (A) Regional map of northwestern North America with the main currents in the Bering Strait and the western Arctic Ocean (based on Grebmeier et al., 2006). (B) Study area [white box in (A)] and surface ocean currents (based on Lin et al., 2020). The black dots represent the grid used for the mean summer sea-ice concentrations. The gray arrows in the lower left corner indicate the two dominant wind directions at Herschel Island – Qikiqtaruk (based on Radosavljevic et al., 2016). The a–b transect marks the section used for the (C) salinity profile with data from the World Ocean Database 2018 (Boyer et al., 2018) using Ocean Data View (Schlitzer, 2018). The thin vertical black lines are the locations of all the CTD measurements (mostly summer to fall measurements) used for the reconstruction of the water mass transect. The dotted lines delimitate approximately the Pacific (31.5–33.5 psu) and Atlantic (>33.5 psu) water masses. (D) Location of core sites in the Herschel Basin and location of two CTD measurements taken in August 2015 (red dot) and April 2016 (blue dot; see Fig. 2). The black lines indicate the northwest–southeast (Fig. A.1) and west–east (Fig. A.2) seismic transects. The main currents are illustrated in (A) and (B) as follows: pink arrow for the Alaskan coastal water, blue arrows for the other Pacific water masses (winter/summer), red dotted arrow for the subsurface Atlantic waters, yellow arrows for the Beaufort Gyre, purple arrow for the coastal flow, and green arrow for the shelf current.

of the Mackenzie River (Environment and Climate Change Canada Historical Hydrometric Database, 2020).

The water masses in summer are strongly stratified on the Beaufort Sea shelf due to the low salinity of the surface waters (Figs. 1C, 2A, light gray zone). The halocline depth ranges between 5 and 10 m depth in summer (Carmack & MacDonald, 2002), and could reach deeper levels according to the summer 2016 Conductivity Temperature Depth (CTD) measurements (Fig. 2A). The temperature and salinity of the surface water layer in summer are 8–9°C and 21–22 psu, respectively, while they are close to the freezing point and 32–33 psu below the halocline (Fig. 2A).

The cold and saline bottom waters of the Herschel Basin originate from upwelling of waters at the shelf break (Fig. 1C) via the Mackenzie Trough (Fig. 1B) and brine rejections from sea-ice formation (Williams & Carmack, 2012; Fig. 2, dark gray zones). As the land-fast ice forms in October up

to the freshet season in June, the stratification breaks down as the water column homogenizes (Fig. 2B).

WINDS AND SEA ICE

Local winds are an important parameter in nearshore ecosystems, as they act as the main drivers of water and sea-ice transport (Kulikov et al., 1998; Frey et al., 2015; Lin et al., 2020), thus controlling sediment and nutrient transport. The important intra- and inter-annual environmental variability in our study area reflects this close relationship to local winds. Around Herschel Island – Qikiqtaruk, strong winds originate either from the northwest or from the east-southeast (Radosavljevic et al., 2016; Fig. 1B). During periods of dominant westerly winds, the Mackenzie River plume and the sea ice remain nearshore. In contrast, dominant easterly winds lead to offshore spreading of the
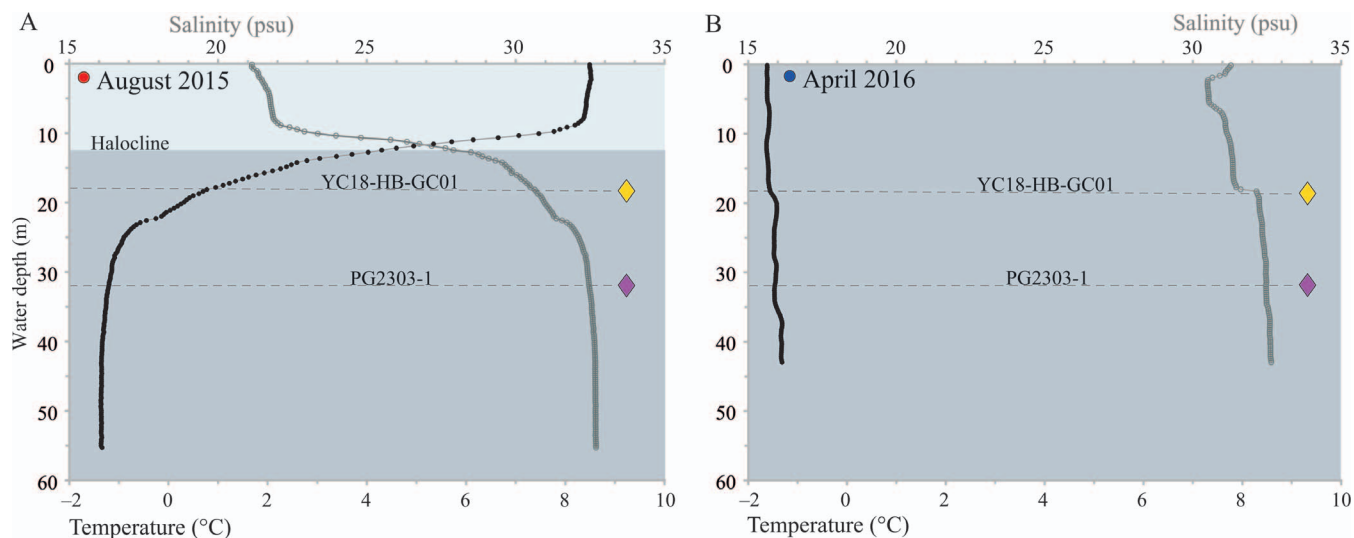
FIGURE 2. Salinity and temperature profiles in the Herschel Basin in August 2015 (A) and April 2016 (B) from CTD data measured with a hand-held CastAway-CTD device. Yellow and purple diamonds mark the water depth of cores YC18-HB-GC01 and PG2303-1, respectively. The brackish summer surface waters (<28 psu) are indicated by the light gray zone. The darker gray zones illustrate waters composed of a mix of brines and upwelled water from the shelf break (mostly Pacific waters). The red and blue dots refer to the location of the CTD measurements shown in Figure 1D.

Mackenzie River plume and foster sea-ice spreading and up-welling (Carmack & MacDonald, 2002; Pickart et al., 2011; Wood et al., 2015), thus enhancing regional primary productivity (Tremblay et al., 2011, 2012; Pickart et al., 2013). The sea ice that interacts with marine currents, upwelling, and vertical mixing (Barber et al., 2012; Schulze & Pickart, 2012; Williams & Carmack, 2015) also plays a protective role along the coastline (Günther et al., 2015).

MATERIAL AND METHODS

SEA ICE

We calculated the mean summer sea-ice concentration in the study area as the average daily sea-ice concentrations in June through September of each year. A breakpoint analysis on the 1979–2017 data highlights a shift in the mean in 2006 CE. Between 1979 and 2006 CE, summer sea-ice concentrations varied from 55% down to 5% with a mean of 31%. After 2006 CE, it stabilized around 7–16% with a mean of 13% (Fig. 3).

SEDIMENT CORES

This study is based on the analysis of two sediment cores collected in the Herschel Basin: core YC18-HB-GC01 (hereafter HBGC01) and core PG2303-1. The HBGC01 core is from the western part of the Herschel Basin (69.544°N, 138.970°W; 18 m water depth), while core PG2303-1 was retrieved from the deeper part of the basin (69.513°N, 138.895°W; 32 m water depth; Fig. 1D).

Acoustic Survey

Hydro-acoustic data were acquired using a Knudsen sub-bottom profiler (12 kHz; Figs. 1D, A.1, A.2). The acoustic image crossing the shelf (NW–SE transect; Fig. 1D) displays faintly laminated to chaotic reflections above 16 m

water depth that evolve downslope into finely laminated reflections below the slope break. This lateral variation of acoustic facies suggests a transition from littoral coarse sediments to fine sediments (Fig. A.1). Thus, the HBGC01 core was collected at the slope below the littoral platform. For the PG2303-1 core site (E–W transect; Fig. 1D), acoustic data show high-amplitude and parallel reflections interpreted as clastic mud (Fig. A.2).

Core Description

The 40-cm long HBGC01 core was retrieved using a UWITEC gravity corer deployed from a zodiac during the 2018 Nunataryuk Yukon Coast expedition on August 9th. The core was stored at 3°C and cut in halves lengthwise at Université Laval, Canada, where the lithological analyses were performed. One half-core was subsampled at 1-cm intervals for micropaleontology and dating (this study). The 20-cm long PG2303-1 core was retrieved on April 20th, 2016, with a UWITEC gravity corer from a tripod on the sea ice during a winter expedition led by the Alfred Wegener Institute. The core was stored cool in a refrigerator and subsampled at 1-cm intervals with a vertical extrusion system. Thus, the short core PG2303-1 was not cut lengthwise, and a descriptive lithology is not available.

The HBGC01 core was photographed and scanned for 3D imagery and density by X-rays Computed-Tomography Scanner (CT-scan) at INRS-ETE facilities using a SIEMENS Somatom Definition AS128 (e.g., Fortin et al., 2013, Figs. 4A, A.3) with the settings adjusted to 165–175 kV and 250–300 mA s^{-1}. We used the ImageJ software (Rasband, 2018) to export and process the raw DICOM format images.

The samples of core HBGC01 were analyzed for grain size at the Laboratoire de géomorphologie et sédimentologie of the Université Laval using a Spectrex Particle counter paired with a Horiba laser diffraction particle size analyzer
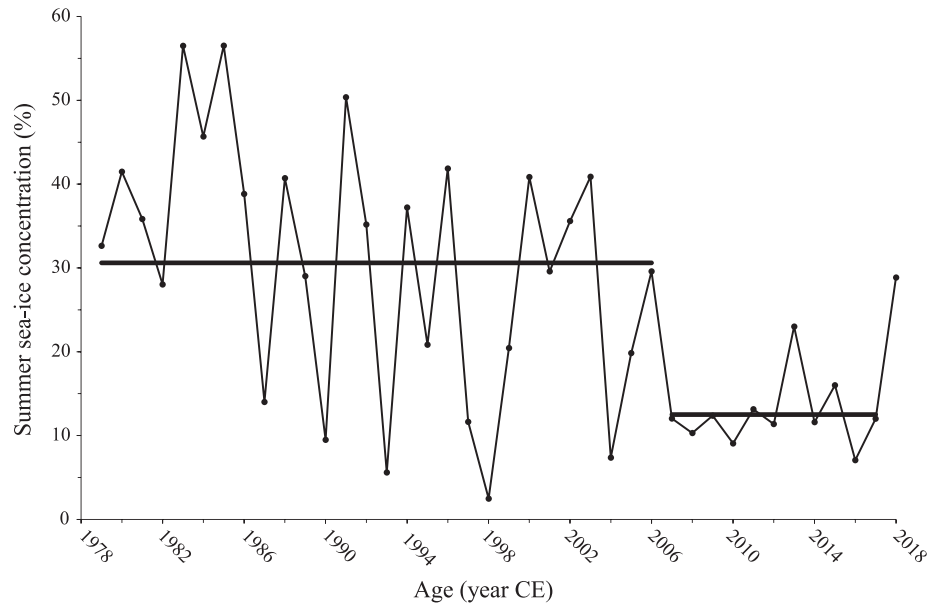
FIGURE 3.   Summer (JJAS) mean sea-ice concentrations (%) calculated from 18-grid points of 25 km × 25 km covering the study area (see Fig. 1B; data compiled from NOAA/NSIDC climate data record of passive microwave sea-ice concentration; cf. Meier et al., 2017). The horizontal black lines mark the mean of the 1979–2006 CE and of the 2007–2017 CE intervals.
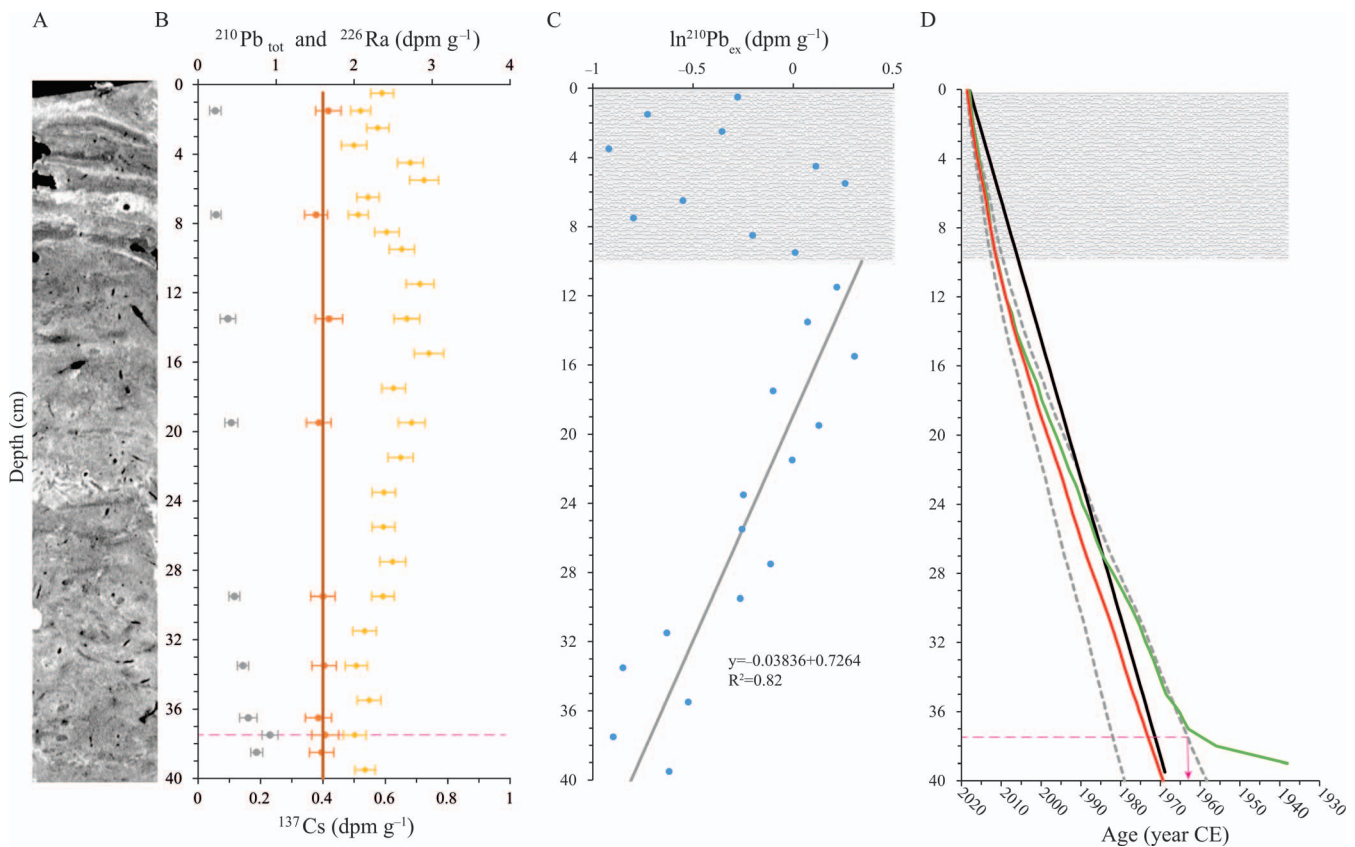

FIGURE 4.   (A) The CT-scan of core HBGC01 with (B) the $^{210}Pb_{tot}$ (yellow), ^{226}Ra (orange), and ^{137}Cs (gray) activity profiles in core HBGC01. The dark orange line marks the ^{226}Ra average ($^{210}Pb_{sup}$) and the pink dotted line marks the depth of maximum ^{137}Cs activity. (C) Natural logarithm of $^{210}Pb_{ex}$ (blue dots). The gray line marks the linear regression of the $\ln^{210}Pb_{ex}$ below 10 cm. (D) HBGC01 core age models obtained with Plum (mean ages = red line; minimum and maximum ages = gray dotted lines), with the CFCS model (black line) and with the CRS-piecewise model (green line; see Fig. A.4 for the original age model graph produced by Plum). The pink arrow marks the age of the nuclear weapon test (1963 CE; Aoyama et al., 2006). The gray shaded areas in (C) and (D) represent the proposed mixed layer.

allowing for grain-size measurements between 0.01 and 3000 μm. The samples of core PG2303-1 were processed at the Université du Québec à Montréal (UQAM) using a Microtrac MRB Bluewave laser diffraction instrument, which can detect grain sizes from 0.01 to 2000 μm. Prior to the measurement, the samples were treated with hydrogen peroxide (30%) to dissolve organic matter. Data were processed in GRADISTAT (Blott, 2010), which defines sand as particles between 2 mm and 63 μm, silt between 63 μm and 2 μm, and clays <2 μm.

Chronology and Sedimentation Rates

The age models are primarily based on ^{210}Pb analyses (raw data in Carnero-Bravo et al., 2021). The measurements procedure of ^{210}Pb followed Baskaran & Naidu (1995), assuming its secular equilibrium with ^{210}Po and using a spike of ^{209}Po. Sediment samples were digested with three acid solutions, successively (HNO_3; HCl, HF, and HNO_3; H_2O_2 and HNO_3). Residues were dissolved in a solution of HCl 0.5 N with ascorbic acid as a reducing agent for Fe. Both ^{210}Po and ^{209}Po were finally deposited (plating) on a silver disk. The measurement was performed by alpha spectrometry using ORTEC^{TM} detectors and the Maestro^{TM} data acquisition software.

We obtained ^{226}Ra and ^{137}Cs activity (γ-emitters) by high-resolution gamma spectrometry using a germanium detector (ORTEC). The efficiency calibration was calculated based on the Columbia River Basalt reference material (BCR-2; USGS). ^{226}Ra was used to estimate the supported ^{210}Pb fraction (^{210}Pb$_{sup}$), in which ^{210}Pb$_{sup}$ is the average of all measurements of ^{226}Ra. The unsupported ^{210}Pb (^{210}Pb$_{ex}$) is the result of the total ^{210}Pb (^{210}Pb$_{tot}$) minus the ^{210}Pb$_{sup}$.

The age models were made using the Plum software (Aquino-López et al., 2018) under R (R Core Team, 2021) and compared with the Constant Flux Constant Sedimentation (CFCS) and the Constant Rate of Supply (CRS) model using the serac package (Bruel & Sabatier, 2020). A first order estimate of the accumulation rate (in a cm^{-1} in Plum) of each core was specified prior to running the software. Plum takes into consideration the ^{210}Pb$_{tot}$ activity and density (g cm^{-3}) of each sample, the ^{210}Pb$_{sup}$ value, and the date of coring. Ultimately, the mass accumulation rate (g cm^{-2}a^{-1}) of each sample was calculated by multiplying the sedimentation rates (cm a^{-1}) derived from the Plum runs and the densities (g cm^{-3}) of the sample section (Table A.1). Sedimentation rate uncertainties were obtained by calculating the sedimentation rates of the highest and lowest ages given by the model (Table A.1). Then, the uncertainties of mass accumulation rate were obtained by following error propagation principles.

MICROPALEONTOLOGICAL ANALYSES

Sixty samples, 40 from core HBGC01 and 20 from core PG2303-1, were analyzed for their microfossil content, with special attention paid to benthic foraminifera, ostracods, and tintinnids. For each sample, 6–7 g of dry sediment were wet-sieved at 63 μm at Geotop-UQAM and dried again. Then, the microfossils were observed and picked with a fine brush under a stereo microscope at 40× to 115× magnification. Each sample was scanned in its entirety, but to ease the

work process, the 63–106 μm and >106 μm fractions were counted separately. In samples containing high concentrations of fine sand, we used a solution of tetrachlorethylene (C_2Cl_4) with a specific gravity of 1.6 g cm^{-3} to separate mineral particles from biogenic remains (Table A.2).

Benthic foraminifera, including calcareous and agglutinated taxa, were identified based on Feyling-Hanssen et al. (1971), Polyak et al. (2002), and Scott et al. (2008b). Identification was made at species level (Table 1; Figs. 5–7), except for the Polymorphinoidea superfamily (hereafter polymorphinids), which has a high diversity of species with poorly known ecology.

Ostracods were identified to genus or species level (Table 2; Figs. 8, 9) based on Gemery et al. (2017) and Stepanova et al. (2003). Specimens identified only to genus level were mainly early instars (molts on juvenile specimens). The ostracod taxa that can tolerate low salinity (<30 psu) and the taxa that prefer salinity >30 psu (euhaline) were distinguished based on Olausson (1982), McDougall et al. (1986), Stepanova et al. (2003, 2019), Tian et al. (2020), and Gemery et al. (2017, 2021; see Table 2).

The agglutinated loricas of tintinnid were all identified as belonging to *Tintinnopsis fimbriata* (Meunier, 1919), which was re-described by Agatha (2008; Table 3). It is important to mention that the lorica of *T. fimbriata*, usually 48–74 μm in length (Agatha, 2008), can be smaller than the sieving mesh size used here (63 μm). Hence, our *T. fimbriata* counts probably provide an underestimation of the population.

Other microfossils recovered in lower numbers in the >63 μm fraction include bisaccate pollen grains (*Picea* spp.), diatoms (*Coscinodiscus* spp.), radiolarians, and planktic foraminifera (Table 3; Fig. 10). The radiolarians were identified as *Spongotrochus glacialis* (Itaki et al., 2003). Being part of the zooplankton dwelling in the open ocean, the radiolarians might be reworked here. Finally, we encountered coccoliths in radiolarian alveoli in one sample (35–34 cm, core HBGC01). The detailed counts of all microfossils are reported in the appendix (Table A.3).

We calculated the concentrations (number of microfossils per gram of sediment; # g^{-1}) for the calcareous and agglutinated benthic foraminifera, ostracods, and tintinnids. Since the size of the observed pollen grains was close to the minimum mesh size (63 μm), if not smaller, we do not report their abundance. The other identified microfossils (diatoms, radiolarians, and planktic foraminifera) were too sparse to calculate concentrations. Fluxes (# cm^{-2}a^{-1}) were obtained by multiplying the mass accumulation rates (g cm^{-2}a^{-1}) with the microfossil concentrations (# g^{-1}). Minimum and maximum fluxes were calculated, taking into consideration the accumulation rate uncertainties.

The assemblages of benthic foraminifera and ostracods are presented in terms of relative abundance (%). Fatela & Taborda (2002) concluded that a minimum of 100 foraminiferal shells are satisfactory for assemblage assessments of dominant taxa (>5%), but that minimum counts should be 300 specimens for the non-dominant taxa. In all samples, the total counts of foraminifera including calcareous and agglutinated is >100 specimens, except for two samples of core HBGC01 (62 and 94 counted specimens in samples 5–4 cm and 4–3 cm, respectively). The required minimum number for ostracod valves was set at 10.

TABLE 1. List of benthic foraminiferal species and genera. * = miliolids; ** = polymorphinids.

Benthic foraminifera	HBGC01	PG2303-1	Figure
Calcareous foraminifera			
Bolivinellina pseudopunctata (Höglund, 1947)	x	x	Fig. 6.9
Buccella frigida (Cushman, 1922)	x	x	Fig. 5.10
Cassidulina reniforme Nørvang, 1945	x	x	Fig. 5.7
Cornuspira involvens (Reuss, 1850)	x	x	Fig. 6.10
Elphidiella groenlandica (Cushman, 1933)	x	-	Fig. 6.2
Elphidium albiumbilicatum (Weiss, 1954)	x	x	-
Elphidium asklundi Brotzen, 1943	x	x	Fig. 5.12
Elphidium bartletti Cushman, 1933	x	x	Fig. 6.1
Elphidium clavatum Cushman, 1930	x	x	Figs. 5.5, 5.9
Elphidium hallandense Brotzen, 1943	x	x	Fig. 5.8
Eoeponidella pulchella (Parker, 1952a)	x	x	Fig. 5.11
Epistominella takayanagii Iwasa, 1955	x	x	-
Haynesina nivea (Lafrenz, 1963)	x	x	Fig. 5.6
Haynesina orbicularis (Brady, 1881a)	x	x	Fig. 6.12
Islandiella helenae Feyling-Hanssen & Buzas, 1976	x	x	Fig. 6.3
Islandiella norcrossi (Cushman, 1933)	x	x	Fig. 6.4
Nonionellina labradorica (Dawson, 1860)	x	x	Fig. 5.1
Pyrgo williamsoni (Sylvestri, 1923)*	x	x	Fig. 5.13
Quinqueloculina stalkeri Loeblich & Tappan, 1953*	x	x	Fig. 6.5
Quinqueloculina seminulum (Linnaeus, 1758)*	x	x	Fig. 5.2
Quinqueloculina lata Terquem, 1876*	x	-	-
Parafissurina himatiostoma Loeblich & Tappan, 1953**	x	x	Fig. 6.8
Polymorphinoidea	x	x	-
Stainforthia feylingi Knudsen & Seidenkrantz, 1994	x	x	Fig. 6.6
Stainforthia loeblichi (Feyling-Hanssen, 1954)	x	x	Fig. 5.4
Stetsonia horvathi Green, 1960	x	x	Fig. 6.11
Triloculina trihedra Loeblich & Tappan, 1953*	x	x	Fig. 5.3
Vaginulina trondheimensis (Feyling-Hanssen, 1964)	x	-	-
Valvulineria spp. Cushman (1926)	x	x	Fig. 6.7
Agglutinated foraminifera			
Ammotium cassis (Parker, 1870)	-	x	Fig. 7.1
Cribrostomoides crassimargo (Norman, 1892)	-	x	Fig. 7.8
Eggerelloides advenus (Cushman, 1922)	-	x	Fig. 7.5
Lagenammina difflugiformis (Brady, 1876)	x	x	Fig. 7.2
Portatrochammina karica Shchedrina, 1946	x	x	Fig. 7.6
Recurvoides turbinatus (Brady, 1881b)	x	x	Fig. 7.9
Sigmoilopsis schlumbergeri (Silvestri, 1904)	x	-	-
Spiroplectammina biformis (Parker & Jones, 1865)	x	x	Fig. 7.4
Textularia earlandi Parker, 1952b	x	x	Fig. 7.3
Textularia torquata Parker, 1952a	x	x	Fig. 7.7

TABLE 2. List of ostracod species and genera. References: 1 Olausson (1982), 2 McDougall et al. (1986), 3 Stepanova et al. (2003), 4 Gemery et al. (2017), 5 Stepanova et al. (2019), 6 Tian et al. (2020), 7 Gemery et al. (2021).

| Ostracods	HBGC01	PG2303-1	Low Salinity Tolerant	Euhaline	References	Figure
Cluthia cluthae (Brady, Crosskey & Robertson, 1874)	x	-		x	1, 5, 6	Fig. 9.3
Cytheropteron brastadensis Lord, 1981/*Cytheropteron discoveria* Brouwers, 1994	-	x		x	1, 2, 6	Fig. 9.7
Cytheropteron elaeni Cronin, 1989	x	x		x	2, 4, 5	Fig. 9.4
Cytheropteron sulense Lev, 1972	-	x		x	5	Fig. 9.2
Cytheropteron suzdalskyi Lev, 1972	x	x		x	2	Fig. 9.8
Eucythere spp.: *Eucythere argus* (Sars, 1866); *Eucythere declivis* (Norman, 1865)	x	x	x		5	Figs. 8.3, 8.4
Eucytherura delineata Whatley & Eynon, 1996	x	x		x	4	Fig. 9.5
Heterocyprideis sorbyana (Jones, 1857)	x	x	x		3, 5, 6	Fig. 8.6
Loxoconcha venepidermoidea (Swain, 1963)	x	x	x		2	Fig. 8.7
Paracyprideis pseudopunctillata Swain, 1963	x	x	x		2, 3, 4, 5	Figs. 8.1, 8.2
Rabilimis mirabilis (Brady, 1868)	x	x		x	1, 2, 5	Fig. 9.1
Sarsicytheridea bradii (Norman, 1865)	x	-	x	x	2, 5, 6, 7	Fig. 8.5
Semicytherura complanata (Brady, Crosskey & Robertson, 1874)	x	x		x	6	Fig. 9.6
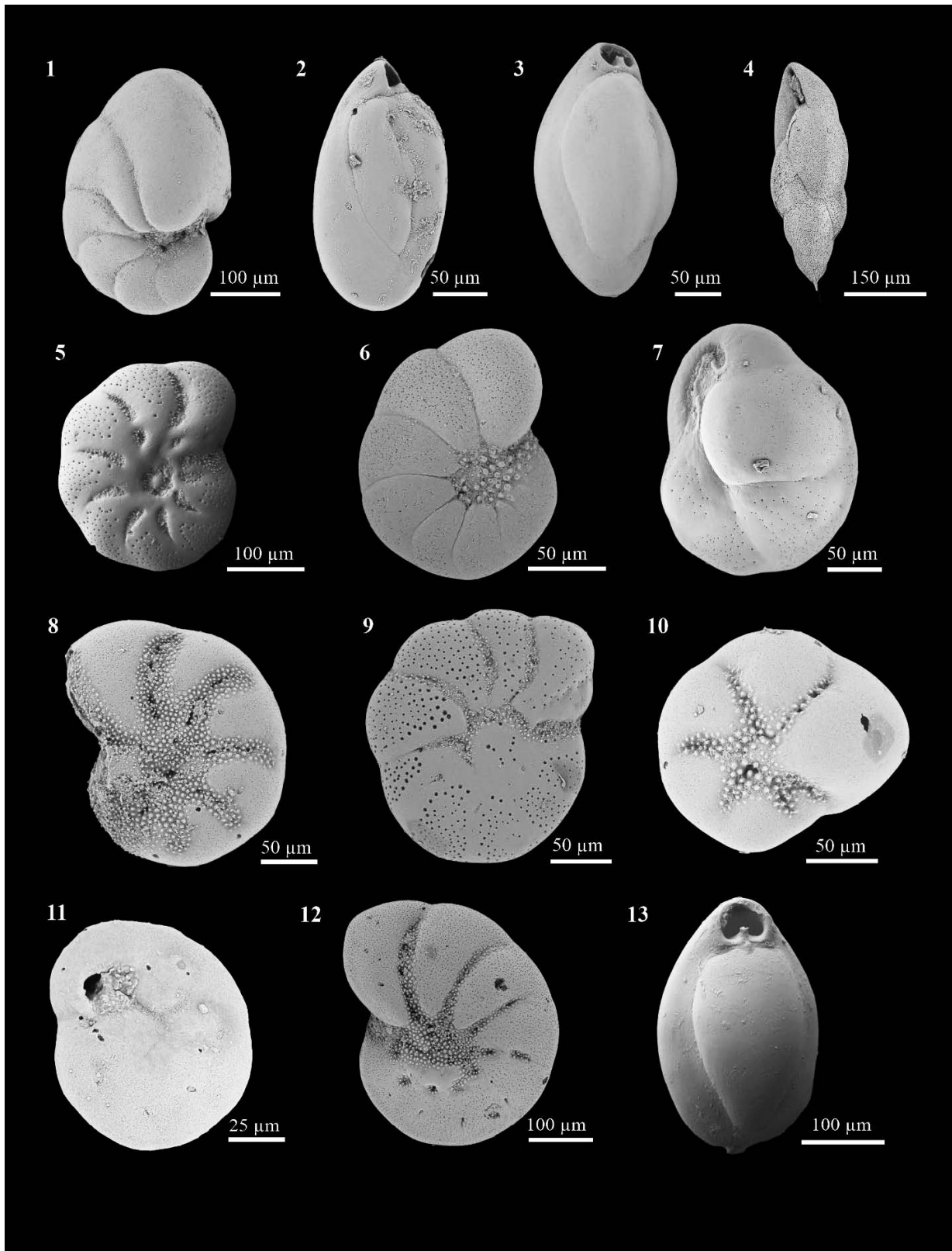
FIGURE 5. Calcareous benthic foraminifera from the Herschel Basin. **1** *Nonionellina labradorica.* **2** *Quinqueloculina seminulum.* **3** *Triloculina tri-hedra.* **4** *Stainforthia loeblichi.* **5, 9** *Elphidium clavatum.* **6** *Haynesina nivea.* **7** *Cassidulina reniforme.* **8** *Elphidium hallandense.* **10** *Buccella frigida.* **11** *Eoeponidella pulchella.* **12** *Elphidium asklundi.* **13** *Pyrgo williamsoni.*
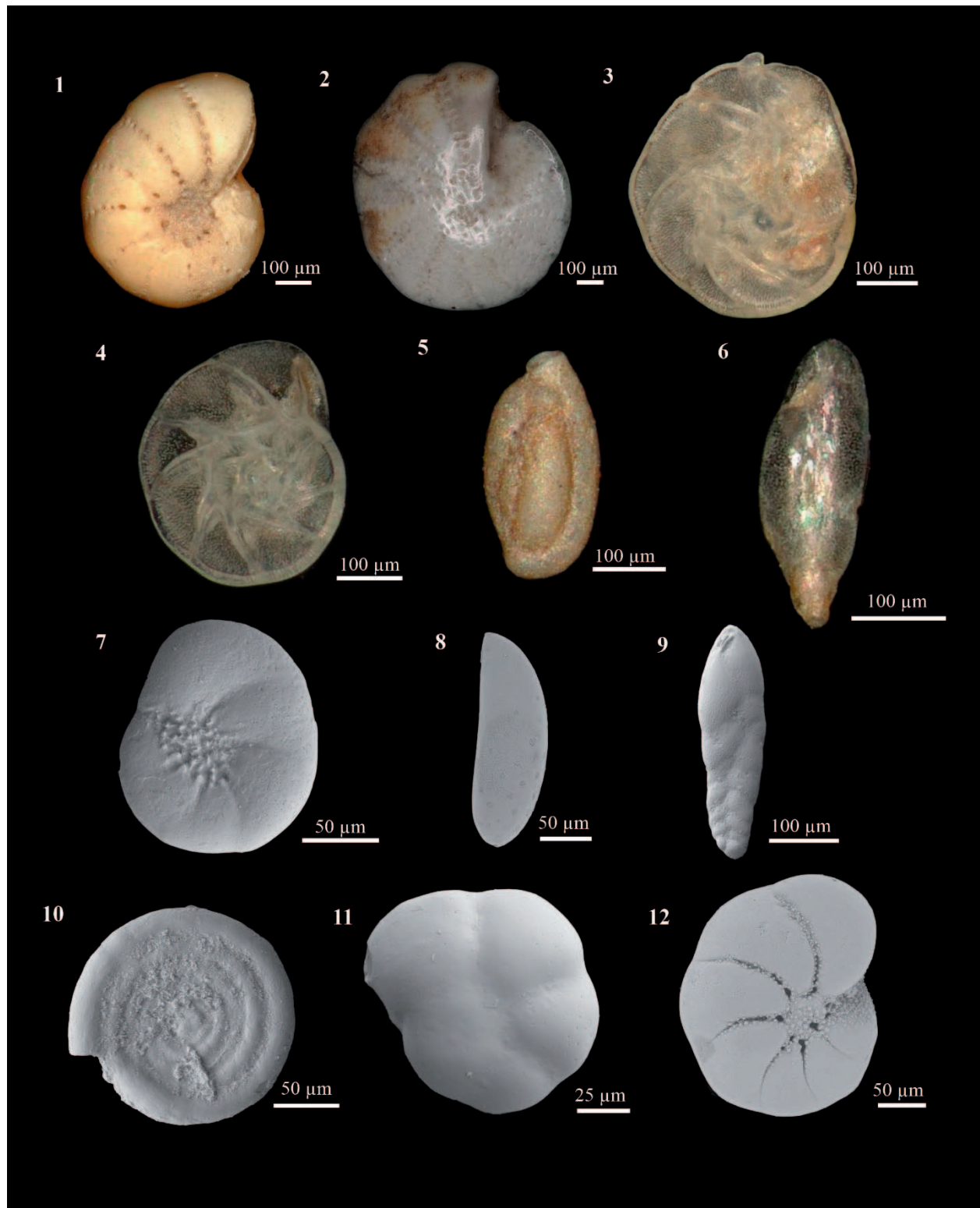
FIGURE 6.   Calcareous benthic foraminifera from the Herschel Basin. **1** *Elphidium bartletti.* **2** *Elphidiella groenlandica.* **3** *Islandiella helenae.* **4** *Islandiella norcrossi.* **5** *Quinqueloculina stalkeri.* **6** *Stainforthia feylingi.* **7** *Valvulineria* sp. **8** *Parafissurina himatiostoma.* **9** *Bolivinellina pseudopunctata.* **10** *Cornuspira involvens.* **11** *Stetsonia horvathi.* **12** *Haynesina orbicularis.*
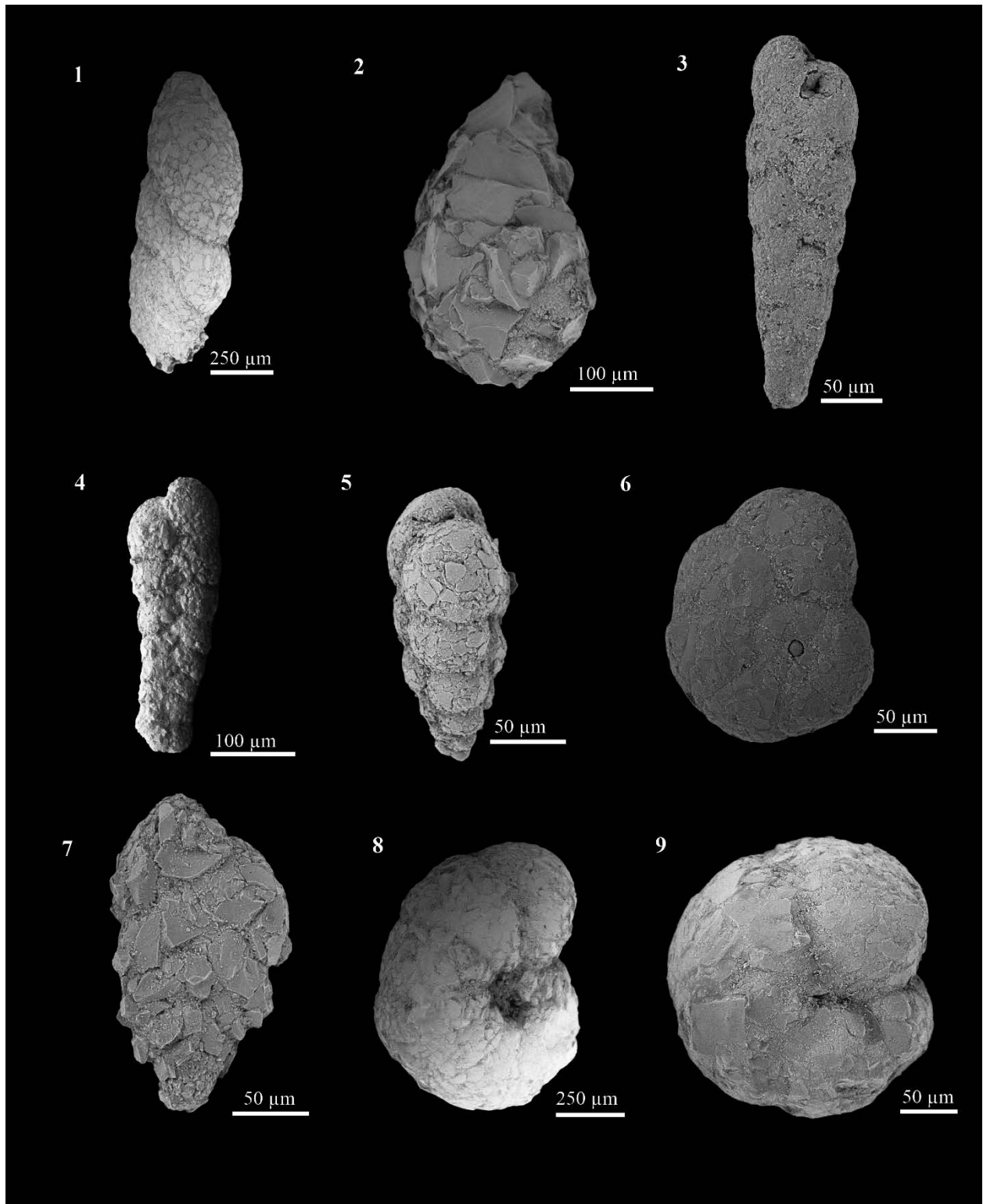
FIGURE 7. Agglutinated benthic foraminifera from the Herschel Basin. **1** *Ammotium cassis.* **2** *Lagenammina difflugiformis.* **3** *Textularia earlandi.* **4** *Spiroplectammina biformis.* **5** *Eggerelloides advenus.* **6** *Portatrochammina karica.* **7** *Textularia torquata.* **8** *Cribrostomoides crassimargo.* **9** *Recurvoides turbinatus.*
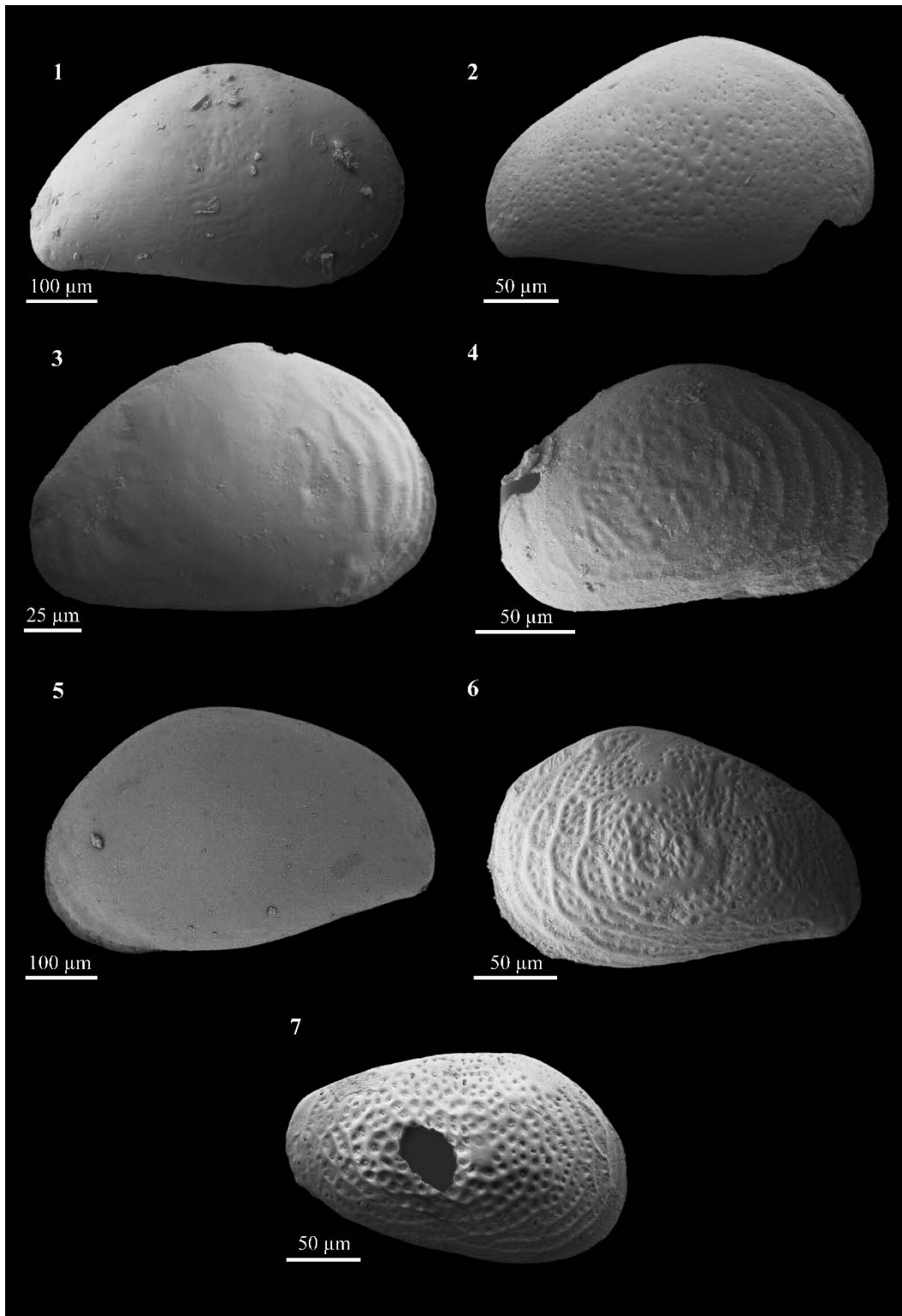
FIGURE 8.   Ostracods from the Herschel Basin. **1, 2** *Paracyprideis pseudopunctillata.* **3, 4** *Eucythere* sp. **5** *Sarsicytheridea bradii.* **6** *Heterocyprideis sorbyana.* **7** *Loxoconcha venepidermoidea* (juvenile).

COMMUNITY DIVERSITY AND STATISTICAL ANALYSES

We calculated the Shannon entropy on the benthic foraminifera and ostracods *Hellinger*-transformed raw counts in the vegan package (Oksanen et al., 2013) under R. The exponential of the Shannon entropy is then used to obtain the Shannon diversity. This diversity considers the abundance and evenness of the species in one sample and is
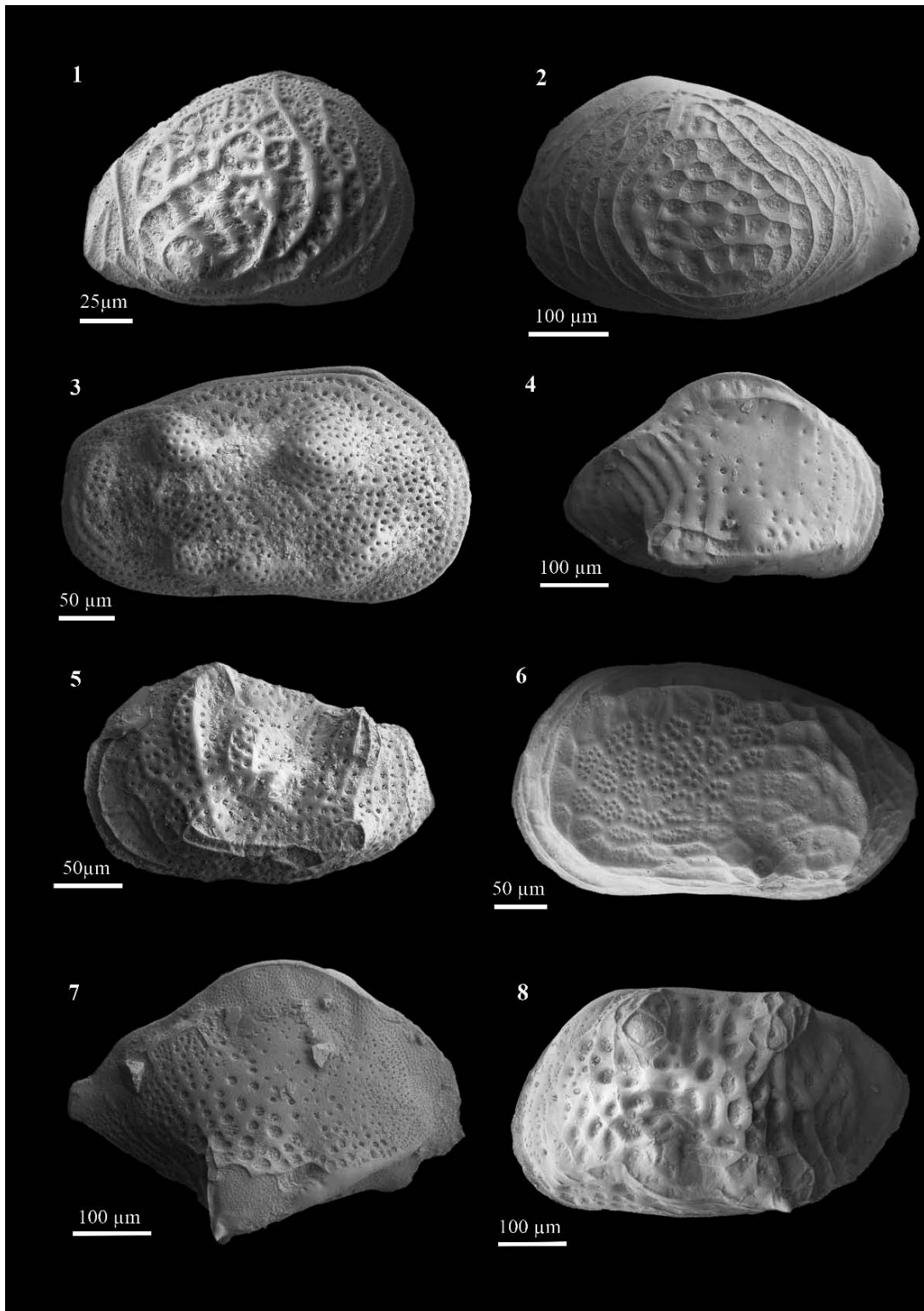
FIGURE 9.   Ostracods from the Herschel Basin. **1** *Rabilimis mirabilis* (juvenile). **2** *Cytheropteron sulense.* **3** *Cluthia cluthae.* **4** *Cytheropteron elaeni.* **5** *Eucytherura delineata.* **6** *Semicytherura complanata.* **7** *Cytheropteron brastadensis/discoveria.* **8** *Cytheropteron suzdalskyi.*
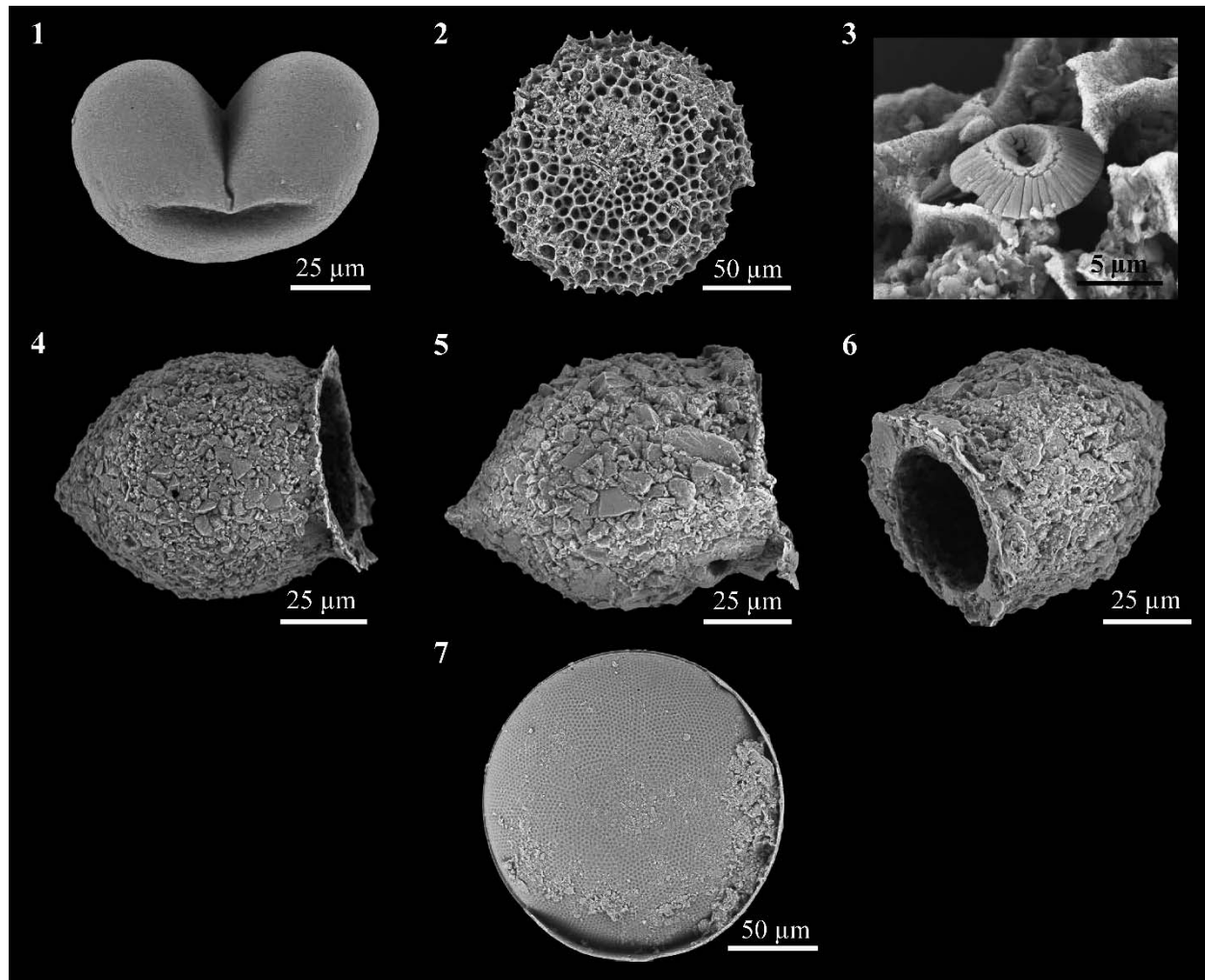
FIGURE 10.   Other microfossils from the Herschel Basin. **1** *Picea* sp. **2** *Spongotrochus glacialis.* **3** *Coccolithus pelagicus.* **4, 5, 6** *Tintinnopsis fimbriata.* **7** *Coscinodiscus* sp.

thus less sensitive to rare species, which seemed appropriate for an Arctic Ocean shelf, where transported allochthonous microfossils from nearshore currents or ice rafting may occur (Wollenburg & Kuhnt, 2000). Among the foraminifera, the polymorphinids remained grouped together for the analysis. Benthic foraminifera not identified to species level were removed from the diversity index calculation but included in the percentage and flux calculations. For ostracods, the Shannon diversity was calculated using identification at the genus level.

Redundancy Analyses (RDAs) were performed using the vegan package under R with the *Hellinger*-transformed raw counts of foraminifera as the response matrix and standardized concentration of sand (%) and microfossil fluxes (for core HBGC01) or microfossil concentrations (for core PG2303-1) as the explanatory variables. For both cores, the RDAs were used to help discriminate ecozones and major shifts in the assemblages. RDAs were not performed on the ostracods due to their low counts especially in core HBGC01 (see section on the Microfossil concentrations and fluxes of core HBGC01).

RESULTS

CORE HBGC01, BASIN MARGIN

Lithology and Grain Size

The sediments in core HBGC01 are brownish gray with sparse presence of millimetric dark laminations. The CT-scan reveals homogenous sediment from the bottom of the core to 10 cm with signs of bioturbation marked by pale mottles and holes (Figs. 4A, A.3). The upper 10 cm show

TABLE 3.   List of other microfossils.

Other microfossils	HBGC01	PG2303-1	Figure
Picea spp.	x	x	Fig. 10.1
Coccolithus pelagicus (Wallich, 1877)	x	-	Fig. 10.3
Coscinodiscus spp.	x	x	Fig. 10.7
Tintinnopsis fimbriata Meunier, 1919	x	x	Figs. 10.4–10.6
Spogontrochus glacialis Popofsky, 1908	x	-	Fig. 10.2

faintly laminated sediments that are discontinuous and of unequal thickness. The content of sand, silt, and clay is almost uniform throughout the record with a mean of $10\pm5\%$, $81\pm4\%$ and $9\pm4\%$, respectively (Fig. 11). Sand content increases to a mean of $17\pm7\%$ in the upper 7 cm with a peak of 31% in the surface sample. The samples mean sediment density is 1.06 ± 0.20 g cm^{-3} (Table A.1).

Radiogenic Isotope Activity and Age Model

The $^{210}Pb_{sup}$ (^{226}Ra average) in core HBGC01 is 1.60 ± 0.05 dpm g^{-1} (disintegrations per minute per gram, Fig. 4B). A log-decrease of $^{210}Pb_{ex}$ can be evidenced between 40 and 10 cm depth (Fig. 4C). Such a behavior supports continuous accumulation of sediments. The $^{210}Pb_{tot}$ in the upper 10 cm shows oscillations of large amplitude (Fig. 4B). Laminations in this layer (Figs. 4A, A.3) suggest pulses of reworked sediments with variable $^{210}Pb_{ex}$ through coastal erosion and nearshore processes (tides, waves, storms, currents, etc.) of shallow-water environments (<20 m; Hill & Nadeau, 1989; Corbett et al., 2006; Hanna et al., 2014). The ^{137}Cs data record a minimum of 0.05 ± 0.02 dpm g^{-1} near the surface and an increasing trend downcore to a maximum of 0.23 ± 0.03 dpm g^{-1} at 38–37 cm. For the Plum model, we considered a mean accumulation (acc. mean) of 1.23 a cm^{-1} by dividing the ^{210}Pb disintegration constant with the slope of the linear regression of log $^{210}Pb_{ex}$ observed between 40 and 10 cm depth (Sanchez-Cabeza & Ruiz-Fernández, 2012; Fig. 4C).

Based on these data, the Plum model provides an age of ~1969 CE at the bottom of the core up to the year of coring (2018 CE) at the surface (Fig. 4D). The mean sediment accumulation rates average 0.8 ± 0.1 g cm$^{-2}a^{-1}$ below 10 cm and are higher but variable above (Fig. 11). The mean estimated age at 38–37 cm is 1973 ± 9 CE (minimum is 1963 CE; Fig. 4D), which coincides with increased ^{137}Cs activity (Fig. 4B) assigned to the maximum nuclear fallout (Aoyama et al., 2006). Although this ^{137}Cs peak is weakly recorded in core HBGC01, it is clearly recorded in a well-dated core collected in the nearby Ptarmigan Bay (Carnero-Bravo et al., 2021; YC18-PB-SC01; Fig. 1D). The Plum output is represented in Figure 4D with the CFCS and the CRS models for which a mixed layer of 10 cm was included. The CRS model was also forced to fit with the 1963 CE ^{137}Cs peak (CRS-piecewise). All three models yield comparable results. Hence, the age model presented here is as robust as possible given all the available radiogenic and lithological data.

Ecological Zonation

Two ecozones are defined in core HBGC01 based on the redundancy analyses of the benthic foraminiferal assemblage, specifically the scores of the first RDA axis (Figs. 12, 13). They are named Ecozone HBGC01-B (1969–2000 CE) and Ecozone HBGC01-A (2000–2018 CE). Details on the two ecozones can be found below.

Microfossil Concentrations and Fluxes

Counts of calcareous benthic foraminifera were >100 in most samples of core HBGC01 (288 ± 134; Table A.3). This corresponds to concentrations of calcareous ben-

thic foraminifera ranging between 8 and 87 foraminifera g^{-1} throughout the record. Agglutinated foraminifera were found in lower numbers (17 ± 14; Table A.3) with concentrations between 0 and 10 g^{-1}. The quasi-continuous presence of agglutinated and calcareous foraminifera suggests generally good preservation.

From 1969 to 2000 CE (Ecozone HBGC01-B), the calcareous foraminiferal concentration averaged to 55 ± 17 g^{-1}. After 2000 CE (Ecozone HBGC01-A), this average decreased to 30 ± 13 g^{-1}. Estimated foraminiferal fluxes are about 37 ± 19 cm$^{-2}a^{-1}$ throughout the record (Fig. 11). Agglutinated foraminifera record a mean concentration of 3 ± 2 g^{-1}, which corresponds to fluxes between 0 and 7 cm$^{-2}a^{-1}$ (Fig. 11). Ostracod concentrations range between 0 and 5 g^{-1} in Ecozone HBGC01-B. Ostracod fluxes are low throughout the record (<3 cm$^{-2}a^{-1}$), particularly in the upper section (2000–2018 CE), where they number <1 g^{-1} of sediment. The mean concentration of *Tintinnopsis fimbriata* is 3 ± 4 g^{-1}. From the bottom of the core to 1996 CE, *T. fimbriata* is five times less abundant (1 ± 1 g^{-1}) than in the 1996 CE to present interval (5 ± 4 g^{-1}). This corresponds to low fluxes until ~1991 CE (<3 cm$^{-2}a^{-1}$) and a mean of 6 ± 6 cm$^{-2}a^{-1}$ afterwards (Fig. 11), with maxima between 2008 and 2014 (11 ± 6 cm$^{-2}a^{-1}$).

The most important feature in the microfaunal record of core HBGC01 is the opposite shifts in *T. fimbriata* and ostracod concentrations at ca. 2000 CE (at the boundary between ecozones HBGC01-B and HBGC01-A; see the last section of the Discussion). We also note that the 2013–2015 CE sediment layer is characterized by maximum calcareous benthic foraminiferal, ostracod, and *T. fimbriata* occurrences, with fluxes reaching up to 119 ± 23 cm$^{-2}a^{-1}$, 2 cm$^{-2}a^{-1}$, and 24 ± 5 cm$^{-2}a^{-1}$, respectively (Fig. 11).

Foraminiferal Assemblages

Twenty-six (26) species of calcareous benthic foraminifera were identified in core HBGC01 (Table 1; Figs. 5, 6). In addition, some specimens were identified to the genus level only (i.e., *Valvulineria* spp.) or grouped as polymorphinids. The dominant species are *Elphidium clavatum* and *Cassidulina reniforme*, with *Eoeponidella pulchella* and *Haynesina nivea* as occasional accompanying species (Fig. 13). A total of seven agglutinated foraminiferal taxa were identified: *Spiroplectammina biformis* and *Textularia torquata* were dominant, while *Textularia earlandi* and *Recurvoides turbinatus* were found occasionally. Rare occurrences of *Lagenammina difflugiformis*, *Portatrochammina karica* (also called *P. bipolaris*), and *Sigmoilopsis schlumbergeri* were noted (Tables 1, A.3; Fig. 7).

The first RDA axis explains 46.5% of the variance. It shows an opposite direction of *Eoeponidella pulchella*, *Haynesina nivea*, and *Quinqueloculina stalkeri* that record negative scores and *Islandiella norcrossi*, *Textularia torquata*, *Stainforthia feylingi*, and *Pyrgo williamsoni* that record positive scores (Fig. 12; see Table 4 for abbreviation corresponding names). Axis 1 also shows an opposite direction of *Tintinnopsis fimbriata* fluxes and percentage of sand on the negative side and ostracod abundance on the positive side. The second RDA axis explains 33.2% of the variance and shows an opposition between most of agglutinated
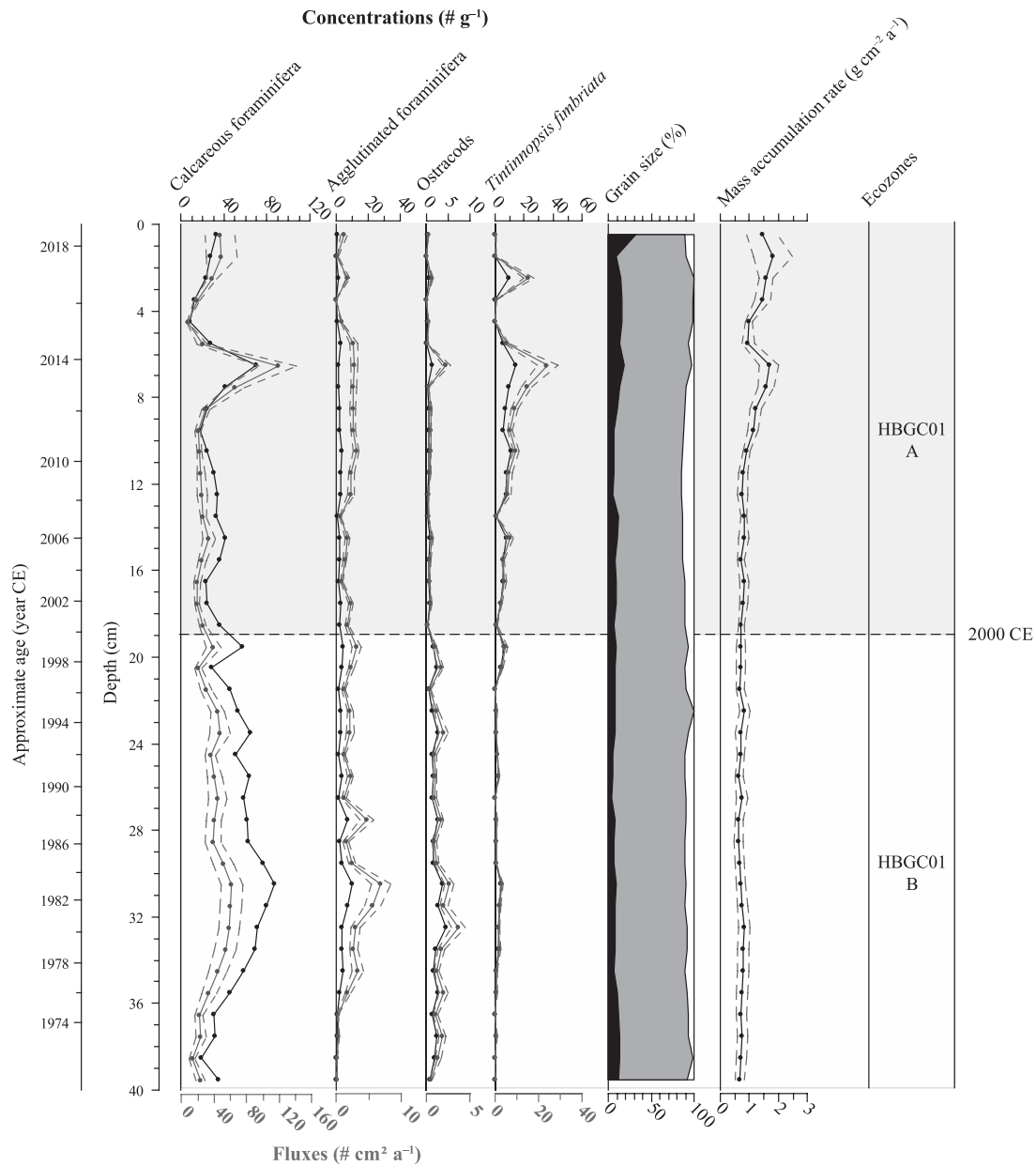
FIGURE 11. Microfossil content (concentrations in black and fluxes in gray), summary grain size data (black = sand; gray = silt; white = clay) and mass accumulation rates in core HBGC01 reported versus depth (cm) and age (year CE). The light gray dotted lines represent the error in accumulation rates and fluxes. The RDA results were used to define the two ecozones.

benthic foraminiferal taxa, which have positive scores, and *Elphidium clavatum*, *Islandiella norcrossi*, and *Cassidulina reniforme*, which have negative scores. Axis 2 is possibly related to microfossil abundances since all microfossil fluxes record positive scores, unlike the sand content.

The species diversity of benthic foraminiferal assemblages is relatively high (Shannon index of 5±1, on average) in core HBGC01 (Fig. 13). *Elphidium clavatum* remains dominant throughout the record (40–65%; Fig. 13). However, the relative abundance of accompanying species records a significant change around 2000 CE when the RDA axis 1 shifts from positive to negative values (Figs. 12, 13) at the ecozone HBGC01-B/A boundary. *Haynesina nivea* and

Eoeponidella pulchella percentages peak synchronously at ~2013 CE, when they together reached 28% of the assemblage (Fig. 13).

Ostracod Assemblages

A total of 11 taxa of ostracods were identified in core HBGC01 (Table 2; Figs. 8, 9). Among those, *Paracyprideis pseudopunctillata* is a recurrent low salinity tolerant (<30 psu) taxon, while *Cluthia cluthae* and *Cytheropteron elaeni* are the dominant euhaline species. In Ecozone HBGC01-B, from the bottom of the core to ~ 2000 CE, *Sarsicytheridea bradii*, *Paracyprideis pseudopunctillata*, and *Cluthia cluthae*
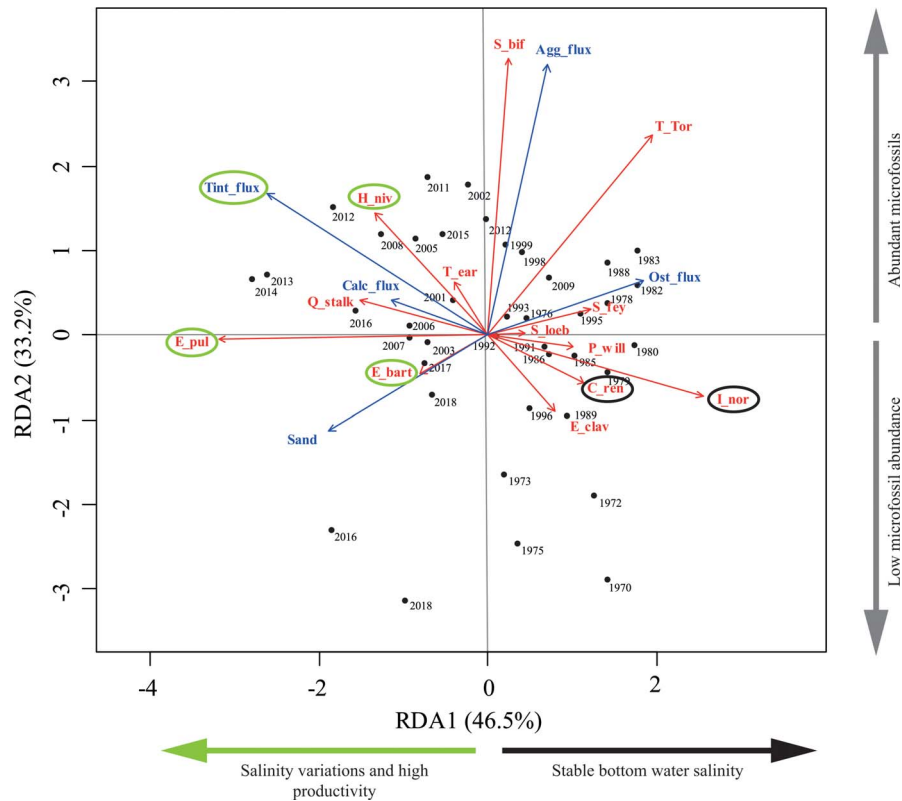
FIGURE 12. Redundancy analysis of the foraminiferal assemblages (red arrows) and the microfossil fluxes and percentage of sand (blue arrows) in core HBGC01. The black dots represent the sample scores on each axis. Indicators of saline waters are circled in dark blue, and indicators of low salinity or high productivity are circled in green. See Table 4 for the abbreviation corresponding names.

TABLE 4. List of abbreviations used in the Figures 12 and 17.

B_frig	*Buccella frigida*
B_pseu	*Bolivinellina pseudopunctata*
C_inv	*Cornuspira involvens*
C_ren	*Cassidulina reniforme*
E_bart	*Elphidium bartletti*
E_clav	*Elphidium clavatum*
E_pul	*Eoeponidella pulchella*
H_niv	*Haynesina nivea*
H_orb	*Haynesina orbicularis*
I_hel	*Islandiella helenae*
I_nor	*Islandiella norcossi*
P_will	*Pyrgo williamsoni*
Q_stalk	*Quinqueloculina stalkeri*
R_turb	*Recurvoides turbinatus*
S_bif	*Spiroplectammina biformis*
S_fey	*Stainforthia feylingi*
S_hor	*Stetsonia horvathi*
S_loeb	*Stainforthia loeblichi*
T_ear	*Textularia earlandi*
T_tor	*Textularia torquata*
Agg_conc	Agglutinated benthic foraminiferal concentrations
Agg_flux	Agglutinated benthic foraminiferal fluxes
Calc_conc	Calcareous benthic foraminiferal concentrations
Calc_flux	Calcareous benthic foraminiferal fluxes
Ost_conc	Ostracod concentrations
Ost_flux	Ostracod fluxes
Sand	Sand concentration (%)
Tint_conc	*Tintinnopsis fimbriata* concentrations
Tint_flux	*Tintinnopsis fimbriata* fluxes

are frequent (Fig. 14) and *Rabilimis mirabilis*, *Eucythere* spp., and *Semicytherura complanata* occur occasionally. This interval is characterized by relatively high diversity with a Shannon index of 4±1. After 2000 CE (Ecozone HBGC01-A), the occurrence of *Eucytherura delineata* increased (Fig. 14), but the general low counts of ostracod valves do not permit statistical assessments.

CORE PG2303-1, DEEP BASIN

Lithology and Grain Size

Although the sediment of core PG2303-1 was not described, the visual description of a long piston core collected at the same location (core PG2303; Fig. A.2) revealed homogenous gray-brownish sediment (Pfalz, 2017). Sediment density measured on core PG2303-1 revealed almost uniform values with a mean of 1.1 ± 0.2 g cm^{-3} (Table A.1), suggesting even water content and low sediment compaction. The core is composed of coarser sediments from 20 to 12 cm, corresponding to ~1998–2005 CE (Fig. 15B), where the sand content reaches a mean of $15\pm9\%$, but the average grain size distribution is $9\pm8\%$ of sand, $72\pm3\%$ of silt, and $18\pm5\%$ of clay (Fig. 16).

Radiogenic Isotope Activity and Age Model

In core PG2303-1, the ^{210}Pb$_{tot}$ activity ranges between 1.8 to 3.0 dpm g^{-1} with an average of 2.6 ± 0.3 dpm g^{-1}
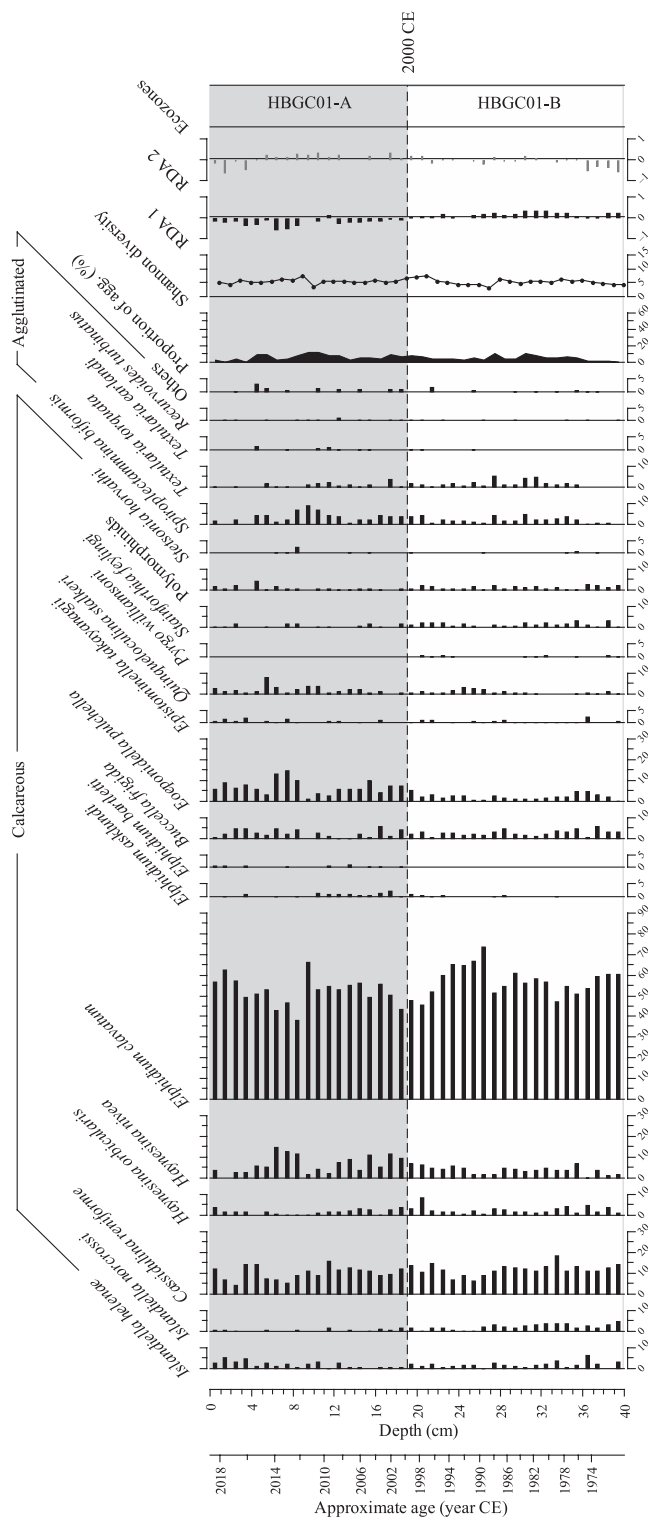
FIGURE 13. Percentages of benthic foraminiferal taxa in core HBGC01 expressed versus depth (cm) and age (year CE). The proportion of agglutinated foraminifera is the percentage of agglutinated foraminifera over the total number of benthic foraminifera (calcareous and agglutinated included). The RDA results were used to define the two ecozones.

(Fig. 15A). $^{210}Pb_{tot}$ decreases down to 1.8±0.1 dpm g^{-1} at 14–13 cm, coinciding with a maximum of sand (31%; Fig. 16). The average ^{226}Ra ($^{210}Pb_{sup}$) is 1.77±0.03 dpm g^{-1}. The ^{137}Cs activity is <0.14 dpm g^{-1} and all measurements overlap taking in consideration uncertainties.

For the calculation of a Plum age model in core PG2303-1, we used the average age at which the incomplete inventory of $^{210}Pb_{ex}$ at 20 cm in core PG2303-1 (17.5 dpm cm^{-2}) was reached in cores HBGC01 and YC18-PB-SC01 (Fig. 1D; Sanchez-Cabeza & Ruiz-Fernández, 2012; Carnero-Bravo et al., 2021) and estimated a mean accumulation rate of 0.83 a cm^{-1}. The Plum model suggests that core PG2303-1 is younger than ∼1998 CE (Fig. 15B), indicating that the entire core corresponds in age only to Ecozone HBGC01-A. However, due to the high apparent sediment mixing the uncertainty in mean accumulation rate, and the short length of the record, we did not interpret the record in terms of age and thus report all results against depth. For the same reason, the mass accumulation rate and microfossil fluxes were not calculated.

Ecological Zonation

Despite the short time span covered by the core, the high sample resolution permitted the definition of three ecozones based on the RDA (Figs. 17, 18). Ecozone PG2303-1-C corresponds to the 15–20 cm core depth interval, Ecozone PG2303-1-B covers from 12 to 15 cm, and Ecozone PG2303-1-A encompasses the upper 12 cm.

Microfossil Concentrations

Counts of calcareous foraminifera range between 208 and 646 specimens per sample (∼6–7 g of dry sediment; mean of 330±149 specimens; Table A.3). More than 50 agglutinated foraminifera were counted in each sample (mean of 80±28; Table A.3). A mean of 11±7 ostracod valves was identified per sample with a maximum of 34. *Tintinnopsis fimbriata* was abundant with >49 specimens counted in each sample. These counts produce mean concentrations of 62±26 calcareous foraminifera g^{-1} and 16±8 agglutinated foraminifera g^{-1}, which suggest good microfossil preservation with depth in the Herschel Basin. Mean ostracod and *Tintinnopsis fimbriata* concentrations are 2±2 g^{-1} and 27±13 g^{-1}, respectively.

There are three abundance peaks of calcareous foraminifera (>80 g^{-1}): at the bottom of the core, at 15–13 cm (approximately corresponding to Ecozone PG2303-1-B), and at 3–1 cm. The agglutinated foraminiferal concentrations do not vary, but the ostracod abundance seems to diminish towards the top of the core, while *Tintinnopsis fimbriata* records maximum concentrations in the upper part of the core (Fig. 16).

Foraminiferal Assemblages

All calcareous benthic foraminiferal taxa observed in core PG2303-1 also occur in core HBGC01 (Table 1; Figs. 5, 6), with 24 taxa in total. As in core HBGC01, *Elphidium clavatum* and *Cassidulina reniforme* are the dominant species throughout the record, comprising 20–35% and 10–20% of the assemblages, respectively (Fig. 18). Accompanying
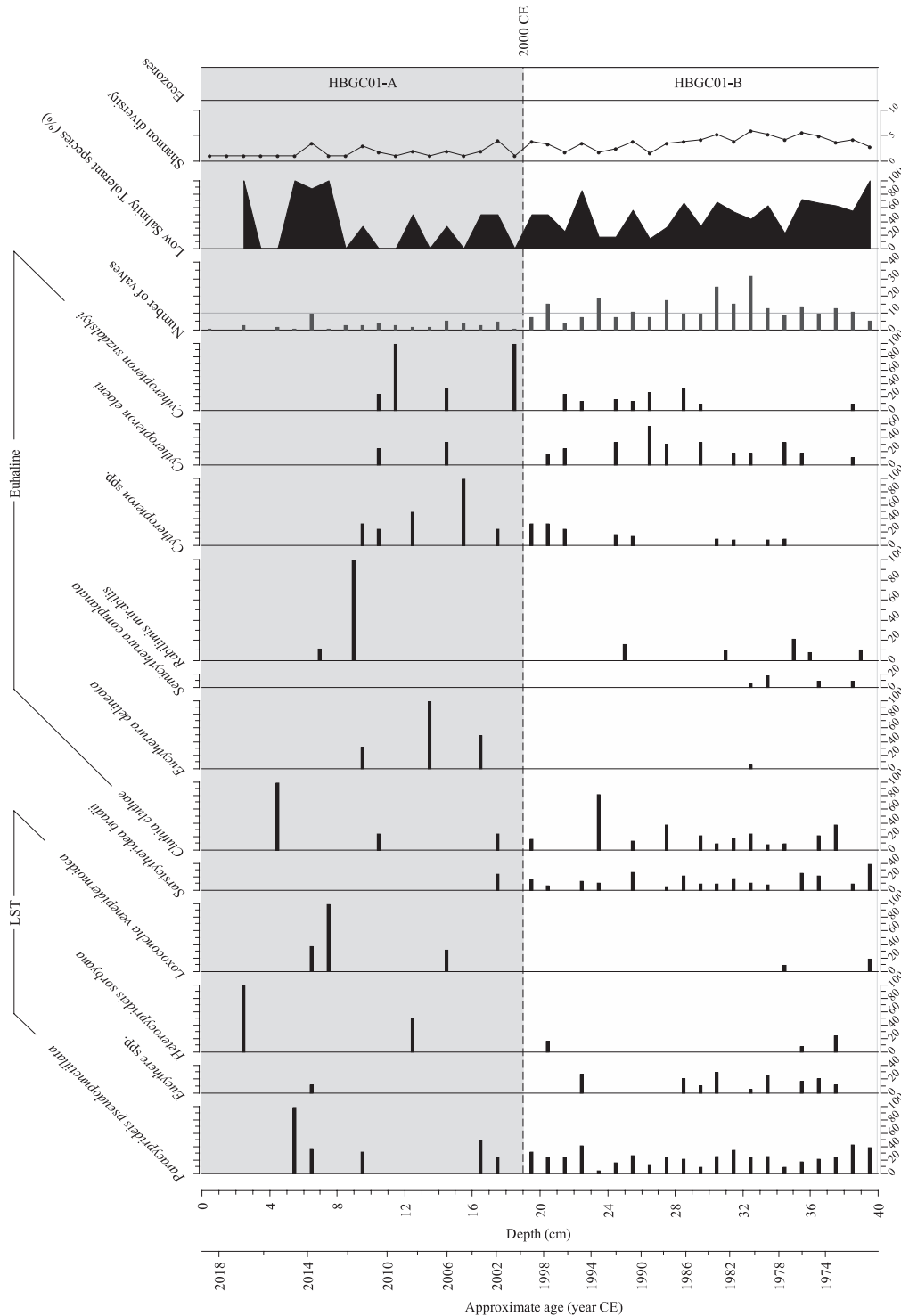
FIGURE 14.   Ostracod assemblages versus depth (cm) and age (year CE) in core HBGC01. Low salinity tolerant taxa (LST) and the euhaline taxa (>30 psu) are indicated. *Sarsicytheridea bradii* does tolerate low salinities (<30 psu), but it is not associated with other LST because it is cosmopolitan, living in a wide range of salinity, temperature and oxygen-level conditions (Stepanova et al., 2019; Gemery et al., 2021). Note that assemblages in the upper 19 cm should be considered with caution, as counts are low; <10 valves per sample. The two ecozones were defined from the RDA of the benthic foraminiferal assemblages and are reported as in Figures 11 and 13.

species are *Haynesina nivea* (5–20%) and *Eoeponidella pul-chella* (5–20%) and to a lesser extent *Stainforthia feylingi* (1–10%) and *Buccella frigida* (0–5%). There are nine species of agglutinated foraminifera, including *Spiroplectammina*

biformis that dominate, together with *Textularia ear-landi*, *Textularia torquata* and *Recurvoides turbinatus*, which are the main accompanying species. The occurrence of other species including *Cribrostomoides crassimargo* and
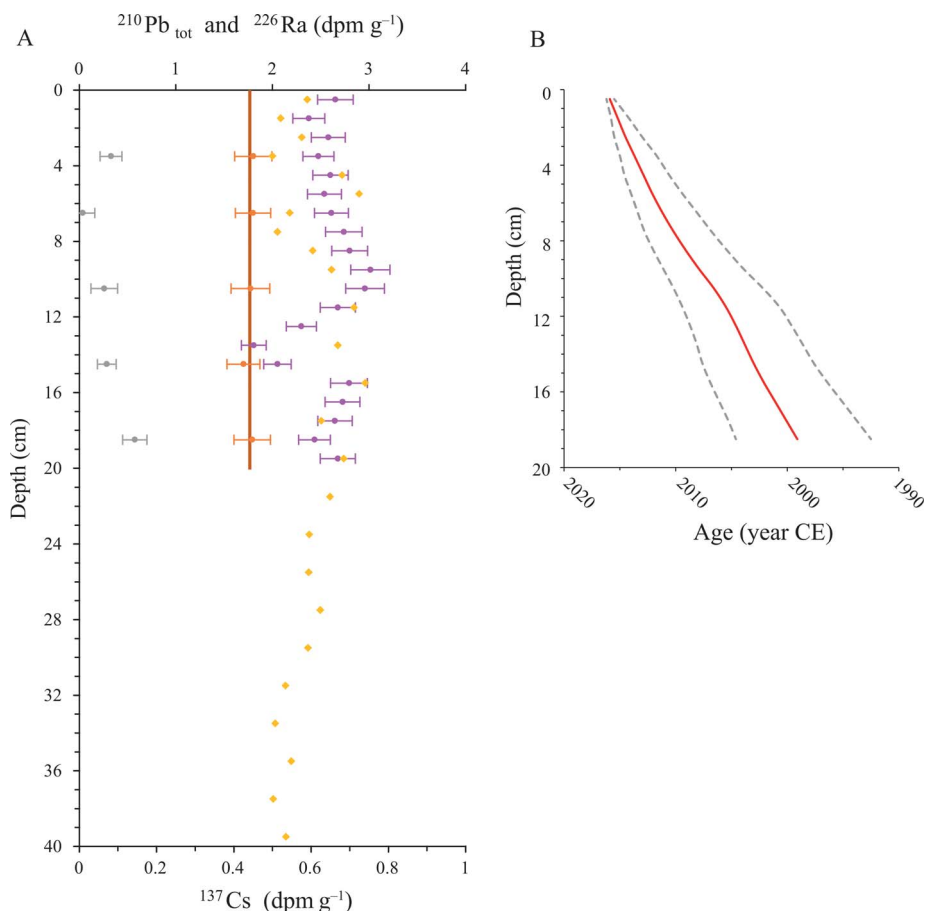
FIGURE 15. (A) ^{210}Pb$_{tot}$ (purple), ^{226}Ra (orange) and ^{137}Cs (gray) activity profiles in core PG2303-1 and the ^{210}Pb$_{tot}$ in core HBGC01 (yellow). The dark orange line marks the ^{226}Ra average (^{210}Pb$_{sup}$) of core PG2303-1. (B) PG2303-1 core age model obtained with Plum including the mean ages (red line) and the minimum and maximum ages (gray dotted lines). See Figure A.5 for the original age model graph produced by Plum.

Eggerelloides advenus is occasional (Tables 1, A.3; Fig. 7). The Shannon diversity index is higher than in core HBGC01 with a mean of 9±2 (Fig. 18).

The RDA reveals an inverse relationship of the abundance of the agglutinated taxa *Spiroplectammina biformis* and *Textularia earlandi* and the calcareous taxa *Elphidium clavatum*, *Haynesina nivea*, *Eoeponidella pulchella*, and *Buccella frigida* on the first axis (40.5% of the variance; Fig. 17; see Table 4 for the abbreviation corresponding names). Accordingly, the concentrations of agglutinated foraminifera have a negative score, while calcareous foraminiferal concentrations score positively. The second axis, which explains 11.5% of the variance, shows an opposite direction of ostracod concentrations, sand (%) and the abundance of numerous foraminiferal taxa on the negative side with *Tintinnopsis fimbriata* concentrations, *Cassidulina reniforme* and *Elphidium clavatum* on the positive side (Fig. 17).

In Ecozone PG2303-1-C, from 20 to 15 cm, the diversity is the highest of the core (Shannon diversity index >10; Fig. 18). Thus, the RDA Axis 2 scores negatively as several taxa reach maximum percentages, including *Islandiella norcrossi*, *Islandiella helenae*, polymorphinids, and *Recurvoides turbinatus* (Figs. 17, 18). In Ecozone PG2303-1-B, from 15 to 12 cm, the RDA axis 1 is positive due to abundant

Haynesina nivea, *Eoeponidella pulchella*, and *Buccella frigida* (Figs. 17, 18). Finally, in Ecozone PG2303-1-A, from 12 cm to the top of the core, the RDA axis 1 is close to nil, while there is a slight increase of *Cassidulina reniforme* and *Spiroplectammina biformis*, *Quinqueloculina stalkeri*, *Stainforthia feylingi*, and *Textularia earlandi* are also present. In the 8 to 1 cm section, the continuous occurrence of *Stetsonia horvathi* is notable (mean of 3±1%; Fig. 18). The uppermost sample differs from all others with negative RDA axis 1 score, abundant agglutinated taxa and low percentages of *Elphidium clavatum*, together with the disappearance of *Buccella frigida* and *Eoeponidella pulchella*. This atypical assemblage recorded in the upper cm of the core might relate to the winter season rather than mean annual conditions, taking into consideration the very high sedimentation rates and the date of coring (April 2016).

Ostracod Assemblages

The ostracod assemblages in core PG2303-1 contain 11 taxa (Table 2; Figs. 8, 9). Among those, *Cytheropteron brastadensis* (*discoveria*) and *Cytheropteron sulense* are restricted to this core, while *Cluthia cluthae* and *Sarsicytheridea bradii* are exclusive to the HBGC01 core. The most common
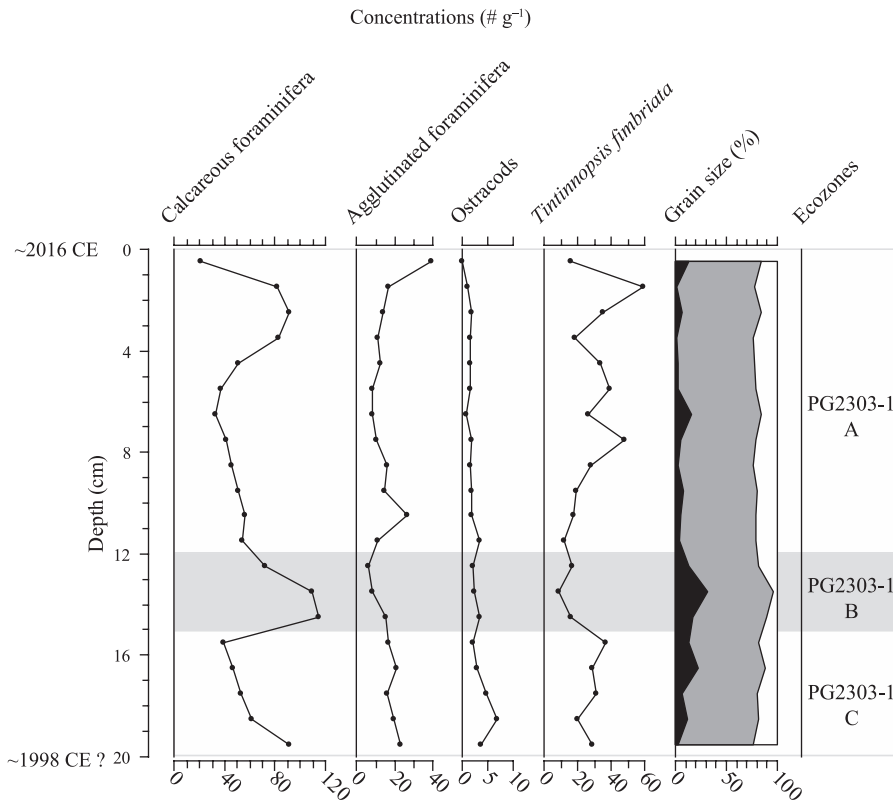
FIGURE 16. Microfossil content and grain size data (black = sand; gray = silt; white = clay) in core PG2303-1 reported versus of depth (cm). The RDA results were used to define the three ecozones.
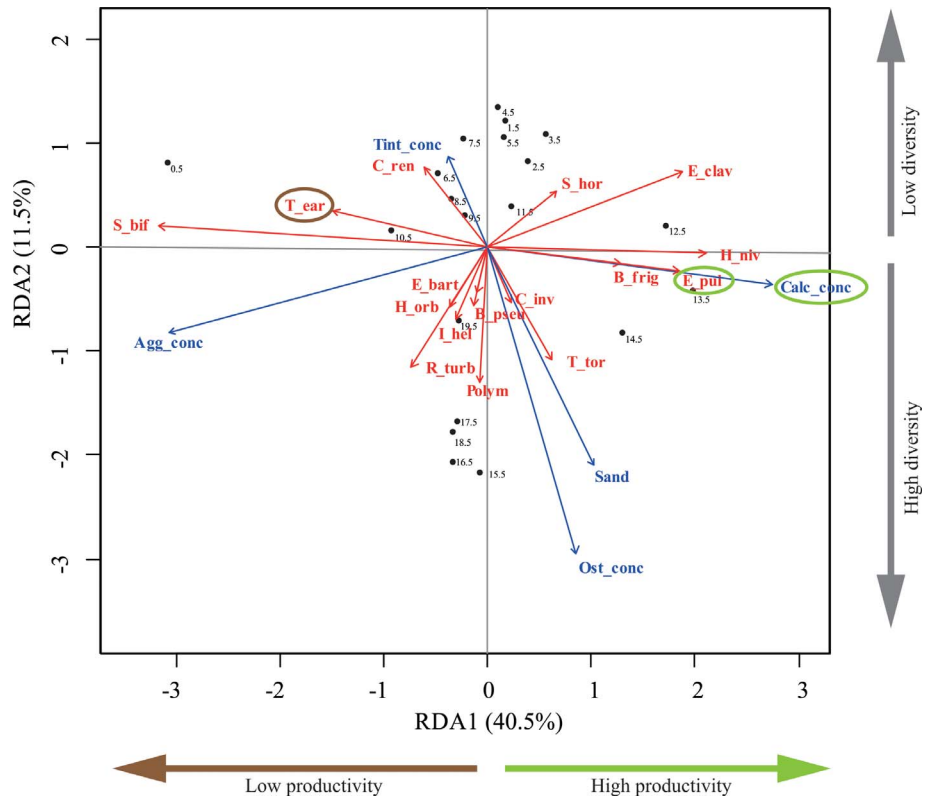
FIGURE 17. Redundancy analysis of the foraminiferal assemblage (red arrows) and the microfossil concentrations and percentage of sand (blue arrows) in samples from core PG2303-1. The black dots represent the sample scores on each axis. Indicators of high productivity are circled in green and of low productivity are circled in brown. See Table 4 for the abbreviation corresponding names.
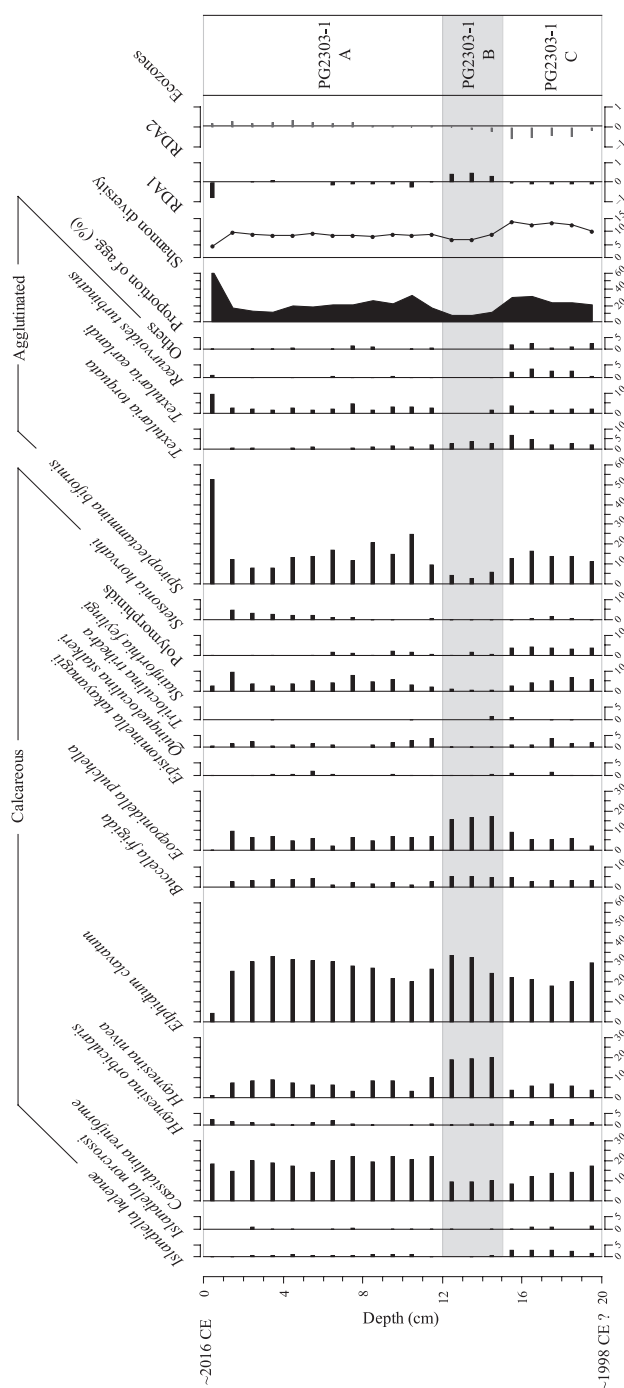
FIGURE 18. Percentages of benthic foraminiferal taxa in core PG2303-1 expressed versus depth (cm). The proportion of agglutinated foraminifera is the percentage of agglutinated foraminifera over the total number of benthic foraminifera (calcareous and agglutinated included). The RDA results were used to define the three ecozones.

species in core PG2303-1 are *Cytheropteron* spp. and *Cytheropteron suzdalskyi*. The mean Shannon diversity index is 2±1. The three ecozones as defined by the RDA of the foraminiferal assemblages (Figs. 17, 18) also reflect changes in the ostracod assemblages. The 20–15 cm interval, Ecozone PG2303-1-C, is dominated by euhaline taxa (Fig. 19), notably *Semicytherura complanata*, *Cytheropteron suzdalskyi*,

and *Cytheropteron* spp., and ostracod concentrations reach maximum values (Figs. 16, 17). From 15 to 12 cm, in Ecozone PG2303-1-B, low-salinity tolerant taxa, including *Heterocyprideis sorbyana* and *Loxoconcha venepidermoidea*, constitute most of the assemblages (Fig. 19). The species diversity is maximum in this interval, as the samples contain both low-salinity tolerant and euhaline taxa. In the first part of Ecozone PG2303-1-A, from 12 to 6 cm, the assemblages are dominated by euhaline taxa, but with low occurrence of *Semicytherura complanata*. Finally, in the upper seven centimeters of Ecozone PG2303-1-A, corresponding to the level where *Stetsonia horvathi* increases in the foraminiferal assemblage (Fig. 18), the ratio between low-salinity tolerant and euhaline ostracods is approximately even.

DISCUSSION

BASIN MARGIN VS. DEEP BASIN

Bottom Water Masses

With a water depth of 18 m, site HBGC01 is located close to the depth of the summer halocline (Fig. 2A). Vertical mixing in response to storm events and tidal dynamics may cause the upper layer (~22–24 psu and >0°C) to mix with the subsurface waters (30 psu and ~0°C; Hill & Nadeau, 1989; Rainville & Woodgate, 2009; Fig. 2A). Hence, the bottom waters at this site may be influenced by the low salinity surface waters that also carry a high concentration of suspended particles either from the Mackenzie River (Doxaran et al., 2015; Ehn et al., 2019; Juhls, 2021) or from terrestrial sources in relation with coastal erosion and resuspension (Klein et al., 2019; Jong et al., 2020). In contrast, core PG2303-1 was retrieved from 32 m water depth, which is significantly deeper than the summer halocline. Consequently, this deep and more offshore site is less likely to be affected by turbidity than the nearshore shallower core HBGC01 (Fig. 1D; see the last section of the Discussion). Turbidity in surface waters could have negative impacts on primary production (Anthony et al., 2004; Retamal et al., 2008; Bonsell & Dunton, 2018; Lewis et al., 2020). In winter, however, below the two-meter-thick land-fast ice, subsurface waters return to saline (32–33 psu) and frigid (<0°C) conditions and sites HBGC01 and PG2303-1 are both bathed by the same water mass, recording values close to the annual mean of the 32 m deep site PG2303-1 (Figs. 2A, B).

In addition to bottom water salinity and turbidity in summer, the two study sites are subject to different bottom current speeds and dynamics. The higher clay content in core PG2303-1 compared to core HBGC01 suggests a higher proportion of suspended sediments deposited by settling in the deeper part of the Herschel Basin, and thus a quieter depositional environment than at the basin margin (Figs. 11, 16). Moreover, the thin laminations in the top 10 cm of the shallow core HBGC01 (Figs. 4A, A.3) could suggest a more dynamic depositional environment, possibly linked to events of resuspension and reworking (Hill & Nadeau, 1984; Corbett et al., 2006; Hanna et al., 2014) during the last decade. Laminations in sediment cores may also refer to oxygen depletion, but supplementary information would be needed to address this assumption.
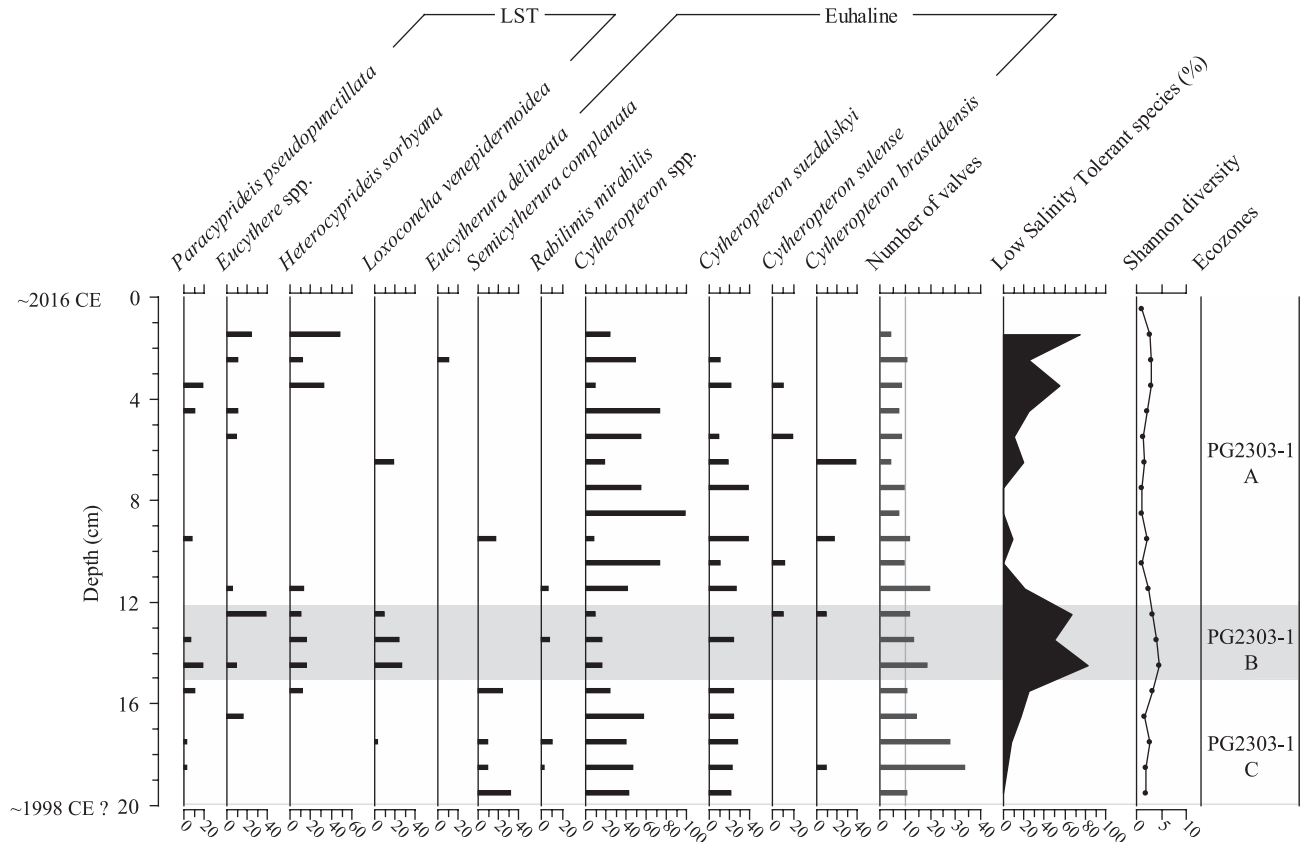
FIGURE 19. Ostracod assemblages versus depth (cm) in core PG2303-1. The low salinity tolerant taxa (LST) and the euhaline taxa (>30 psu) are indicated. Note that occurrences in assemblages with less than 10 valves should be considered with caution. The three ecozones were defined from the RDA of the benthic foraminiferal assemblages and are reported as in Figures 16 and 18.

Microfaunal Assemblages

In general, the benthic foraminiferal and ostracod assemblages of the two studied cores compare well with assemblages described from other Arctic shelf settings (McDougall et al., 1986; Reimnitz et al., 1993; Wollenburg & Mackensen, 1998; Wollenburg & Kuhnt, 2000; Polyak et al., 2002; Scott et al., 2008b, Husum et al., 2015; Gemery et al., 2017). The dominance of *Elphidium clavatum*, the abundance of agglutinated taxa such as *Spiroplectammina biformis* and *Textularia* spp., and the presence of taxa tolerant to low salinity such as *Haynesina orbicularis*, *Buccella frigida*, and polymorphinids, are typical of Arctic shelf environments (Polyak et al., 2002; Scott et al., 2008a; Figs. 13, 18). However, in our study, we report for the first time the occurrence of the accompanying taxon *Haynesina nivea* on the Beaufort Sea shelf. This species has been associated with shallow and low salinity environments (Madsen & Knudsen, 1994; Luoto et al., 2011; Voltski et al., 2015; see section below on sea ice and salinity).

The two sites also show some important differences in the microfossil assemblages. The shallow core HBGC01 holds high relative abundance of taxa tolerant to river proximal and low salinity environment such as *Elphidium clavatum* (cf. Hald & Steinsund, 1996; Hald & Korsun, 1997; Polyak et al., 2002; Knudsen et al., 2008), *Islandiella he-*

lenae (cf. Cage et al., 2021), and *Elphidium bartletti* (cf. Polyak et al., 2002). The occurrence of *Elphidium asklundi* in core HBGC01 probably also suggests a tolerance to low salinities. In contrast, *Cassidulina reniforme*, related to cold and saline conditions (Hald & Korsun, 1997; Polyak et al., 2002), is more abundant at the deeper site of core PG2303-1 (Fig. 18), where euhaline ostracods also dominate (Fig. 19). *Stainforthia feylingi* is also more abundant in core PG2303-1 than in core HBGC01, which might be due to the higher salinities and closer proximity to productive sea-ice margins (cf. Seidenkrantz, 2013) evident for the central Herschel Basin compared to the near-coastal area. The differences in microfaunal assemblages at the two study sites probably reflect the water depth, with increased seasonal salinity gradient and bottom water instability at the shallower site HBGC01, proximal to the summer halocline and wave action. Salinity variations at site HBGC01 may partly control the changes in foraminiferal assemblages, which is illustrated by the low-salinity tolerant taxa *Haynesina nivea* and *Elphidium bartletti* that vary in opposite to *Islandiella norcrossi* and *Cassidulina reniforme* (Fig. 12). However, changes in foraminiferal assemblages in the Herschel Basin would primarily be linked with food supply as shown by the occurrence of *Eoeponidella pulchella*, a foraminiferal taxon indicative of high primary productivity (Knudsen et al., 2008; Wollenburg & Kuhnt, 2000), highly weighted

on the first axis of both cores (Figs. 12, 17). This relationship is especially clear in core PG2303-1, as *E. pulchella* is inversely related to *Textularia earlandi*, a low trophic requirement taxon (Jennings et al., 2020; Fig. 17).

The sediment substrate and bottom currents may also affect the assemblages. The coarser-grained sediments of the shallow core HBGC01 go together with abundant *Elphidium bartletti* (Polyak et al., 2002). The ostracod *Sarsicytheridea bradii*, which is only observed in core HBGC01 (Fig. 14), may also prefer coarser substrates (Gemery et al., 2021). Moreover, *Sarsicytheridea bradii* can tolerate a wide range of salinity, temperature, and oxygen levels (Stepanova et al., 2019; Gemery et al., 2021), which better corresponds to the more variable conditions that likely characterize the shallow HBGC01 core site. Early instars of ostracods are less abundant in core HBGC01 than in core PG2303-1 (mainly *Cytheropteron* spp.; Figs. 14, 19), which also suggest a higher-energy environment in the basin margin (Whatley, 1983).

High sand content could potentially point to preservation issues and/or unfavorable enhanced bottom currents at the shallow site HBGC01, as it is opposed to microfossil abundances, especially agglutinated foraminifera (Fig. 12). This relationship is expressed in a few samples at the core top and in the 1969–1975 CE interval (Figs. 11–13). Similarly, particularly abundant sand in Ecozone PG2303-1-B (>~10%; Fig. 16) may have negatively affected the preservation condition or productivity of the agglutinated foraminifera (Figs. 16, 18). However, the sand content at the deeper site PG2303-1 seems to be associated to a certain extent with increased primary productivity, as it reaches maximum values in Ecozone PG2303-1-B concurrently with high calcareous foraminiferal concentrations and *E. pulchella* abundances (Figs. 16–18). The sand content is also relatively high in Ecozone PG2303-1-C, accompanied by high ostracod concentrations (Fig. 16) and abundant *Semicytherura complanata* (Fig. 19). Because *Semicytherura complanata* has been associated with polynyas (Stepanova et al., 2003), we hypothesize the presence of a polynya-type environment in Ecozone PG2303-1-C with enhanced brine rejections that lead to vertical mixing (Smith & Morison, 1998) and oxygenated bottom waters, in addition to high salinity. Accordingly, *Islandiella norcrossi*, which prefers saline stable bottom waters (Cage et al., 2021), reaches its maximum occurrence (Fig. 18). Such conditions might have contributed to maximum foraminiferal species diversity at the bottom of the Herschel Basin (Fig. 18).

The ~2000 CE Shift

Sea Ice and Salinity

An important shift is recorded in the shallow core HBGC01 at the transition between ecozones HBGC01-B and HBGC01-A (~2000 CE). It is marked by a transition from abundant *Islandiella norcrossi* and *Cassidulina reniforme* that have preference for salinity >30 psu (Polyak et al., 2002; Cage et al., 2021) to assemblages characterized by *Elphidium bartletti* and *Haynesina nivea* that are both tolerant to low salinity (Fig. 13; Madsen & Knudsen, 1994; Polyak et al., 2002; Luoto et al., 2011; Voltski et al., 2015).

Hence, the shift at ~2000 CE seems to correspond to a transition from a relatively stable and saline environment to an environment marked by lower salinity and unstable conditions. The occurrence of *H. nivea* seems particularly significant to explain this transition. Hence, in modern assemblages of the Scoresby Sound and the White Sea, *H. nivea* was retrieved in very shallow environments (<10 m), where high seasonal fluctuations occur with warm and low saline summer surface waters and currents fostering high sand content (Madsen & Knudsen, 1994; Voltski et al., 2015). In paleoceanographic studies, this species was often related to shallow marine environments (Feyling-Hanssen & Ulleberg, 1984; Hansen & Knudsen, 1995; Luoto et al. 2011). In Ecozone PG2303-1-B, *H. nivea* reaches maximum values concomitantly with low salinity tolerant ostracod taxa such as *Loxoconcha venepidermoidea* and *Heterocyprideis sorbyana* (Figs. 18, 19).

At the shallow site HBGC01, sea ice may foster stable conditions in the bottom water, as it is a natural barrier for waves and winds (Overeem et al., 2011; Schulze & Pickart, 2012). The transition towards lower mean summer sea-ice concentrations after 2006 CE (Fig. 3) follows slightly the shift in microfaunal assemblages dated at 2000±4 CE and appears closely synchronous with the near-disappearance of *Islandiella norcrossi* (Fig. 13). The benthic foraminifera *I. norcrossi* in the lower part of core HBGC01 could thus be an indirect indicator of sea ice-induced stratification and increased bottom-water stability at this site prior to 2006 CE. In contrast, the high sand fraction may indicate increased bottom water instability from wind-induced nearshore currents and wave action in longer ice-free seasons towards the present (Fig. 11), which could have generated reworking and resuspension in the surface sediment (10–0 cm; Figs. 4A, A.3; see the Radiogenic isotope and age model section of core HBGC01).

Eoeponidella pulchella and Productivity

A significant microfaunal change in Ecozone HBGC01-A is indicated by the high percentages of *Eoeponidella pulchella* in this zone (Fig. 13). In modern assemblages, *E. pulchella* is common on Arctic shelves and shelf breaks (Wollenburg & Mackensen, 1998; Wollenburg & Kuhnt, 2000; Scott et al., 2008b; Griffiths, 2010), but was also found in the Gulf of Mexico (Poag & Tresslar, 1981), and is often linked to high primary productivity. In surface sediments of the Canadian Arctic Ocean, *E. pulchella* constitutes ~9% of the benthic foraminiferal assemblage off Cape Bathurst (59 m; Scott et al., 2008b), known for the advection of saline nutrient-rich upwelled waters (Tremblay et al., 2011; Walkusz et al., 2012). *Eoeponidella pulchella* was also noted as an important species (20% of the living fauna) in the surface sample of core PS2480 in Vilkitsky Strait, Laptev Sea (51 m; Fütterer, 1994; Wollenburg & Kuhnt, 2000), which is characterized by high biogenic silica content (Nürnberg, 1996), chlorophyll-*a* concentrations (Boetius et al., 1996) and marine organic carbon (Boucsein & Stein, 2000). Furthermore, in 1993 CE, the year that core PS2480 was collected, the wind conditions favored upwelling in the Laptev Sea (Janout et al., 2015; Osadchiev et al., 2020). The distribution of *E. pulchella* in surface sediment samples of the eastern Arctic Ocean documented

by Wollenburg & Kuhnt (2000) also supports a strong link to high primary productivity.

In our study, the maximum foraminiferal concentrations occurred concurrently with peaks in *E. pulchella* at ~2013 CE in core HBGC01 (Figs. 11–13) and in Ecozone PG2303-1-B (Figs. 16–18), which suggests high benthic foraminiferal fluxes linked to high primary productivity. Wollenburg & Kuhnt (2000) argued that assemblages of benthic foraminifera provide a better indication of trophic level than foraminiferal concentrations due to preservation issues. Still, in our study, the good preservation of foraminiferal shells throughout the sequences allows us to consider the total concentrations and fluxes of benthic foraminifera as a valuable productivity indicator in the Herschel Basin. We also conclude that *E. pulchella* is an excellent indicator of productivity in the Herschel Basin. However, at present it is not clear if the high productivity is due to longer sea ice-free seasons (Fig. 3), the replenishment of nutrient-rich Pacific waters, increased organic carbon from rivers and coasts, or a mix of all the above (more specifications in the last section of the Discussion).

Tintinnopsis fimbriata and Suspended Particulate Matter-Rich Freshwater

A special feature in the micropaleontological records of the shallow core HBGC01 is the high *Tintinnopsis fimbriata* fluxes, particularly pronounced after 2008 CE. This coincides with enhanced *T. fimbriata* concentrations at the end of Ecozone PG2303-1-A (<9 cm; Figs. 11, 16). Concentrations of *T. fimbriata* can be underestimated due to their small size. However, specimens tend to be bigger when they are abundant (Rogers et al., 1981), as observed for several tintinnid species (Dolan et al., 2014). The lower abundance of *T. fimbriata* before 1996 CE is likely not due to poor preservation as it occurs downcore together with abundant agglutinated foraminifera (Fig. 11). Hence, the increase in *T. fimbriata* fluxes after 1996 CE at the basin margin presumably reflects a real increase in tintinnid abundance.

According to previous studies, *T. fimbriata* occurs in nearshore areas near river mouths (Echols & Fowler, 1973; Burkovsky, 1976; Rogers et al., 1981). It was probably observed in sediments from the Beaufort Sea shelf by Scott al. (2008a, b), who reported it as *Tintinnopsis rioplatensis* (Souto, 1973). Tintinnid abundances in the water column have shown positive correlations with chlorophyll-*a* concentrations (Dolan et al., 2007). Additionally, maximum abundance of *T. fimbriata* occurred in relation to maximum chlorophyll-*a* concentration in a Hudson Bay inlet (Rogers et al., 1981) and early spring bloom in the Bedford Basin (Paranjape, 1987; Li, 2014). However, *T. fimbriata* also reaches peak occurrence during winter in the White Sea (Burkovsky, 1976), when primary production is limited (Chernov et al., 2018), which suggests it could be a low-temperature tolerant opportunistic species. It has also been proposed that the abundance of tintinnids might depend more upon the nature of the prey than the quantity of the food (Dolan et al., 2014).

Preferential occurrence of *T. fimbriata* in river proximal areas could be related to the availability of small mineral particles to build agglutinated lorica (Pierce & Turner, 1993). Scott et al. (2008b) associated the agglutinated tintinnids with the Mackenzie River water discharges, thus to freshwaters rich in suspended particulate matter. Its association with suspended particles is consistent with the concomitant increase of *Quinqueloculina stalkeri*, which is known to tolerate turbidity and to be a bacterial-feeder rather than an algal-feeder (Guilbault et al., 2003; Figs. 11, 13). Hence, *T. fimbriata* might be an indicator of turbid freshwater discharge, but a relationship to primary productivity remains equivocal. The significant increase of *T. fimbriata* after 2008 CE may reflect a western spreading of the Mackenzie River plume to the study site, which could also be related to reduced sea-ice concentration (Fig. 3). The detrital particles used to build their agglutinated lorica might also originate from a more local source related to coastal erosion that has increased since ~2000 CE (Jones et al., 2009; Obu et al., 2016; Radosavljevic et al., 2016).

Ecological Considerations about Eoeponidella pulchella, Haynesina nivea, Tintinnopsis fimbriata, and Ostracod Abundance

The occurrences of *E. pulchella* and *H. nivea* are closely correlated (r = 0.68 and r = 0.78 in cores HBGC01 and PG2303-1, respectively). Both species show increased occurrences in ecozones HBGC01-A and PG2303-1-B, which leads us to suggest a change towards increased productivity concurrently with low salinity excursions. Kutos et al. (2021) already proposed a relationship between benthic productivity and freshwater discharge in the Mackenzie Trough. In our study, the influence of low salinity waters from river discharge is further supported by the abundance of *Tintinnopsis fimbriata* fluxes over the last two decades in the shallow HBGC01 core (Fig. 11).

The main source of freshwater is the Mackenzie River. However, the Mackenzie River is not particularly rich in nutrients compared to other Arctic rivers (Holmes et al., 2011), especially at distal locations from the plume (Emmerton et al., 2008; Tremblay et al., 2014). Nevertheless, the terrigenous organic carbon and/or the microbial activity therein, either from the more distal Mackenzie River or the proximal permafrost thaw, may provide large food sources (Bell et al., 2016; Terhaar et al., 2021). Another source of nutrients originates from the upwelling of nutrient-rich Pacific waters onto the shelf during easterly winds (Tremblay et al., 2011, 2012; Pickart et al., 2013). The Mackenzie River plume reaching the study site and upwelling of deeper waters may both occur during periods of strong easterly winds, which could explain the duality between freshwater and productivity and the co-occurrence of *H. nivea* and *T. fimbriata* with *E. pulchella*.

The rapidly changing environment of the 21st century may also have negative impacts on the microfauna, as suggested by the decrease in ostracod fluxes at the shallow site of core HBGC01 (Fig. 11). From the inverse relationship between ostracod and *T. fimbriata* concentrations (Figs. 11, 16), we suggest that an increased supply of low salinity waters rich in suspended particulate matter at the HBGC01 site is unfavorable for ostracods. Because low salinity is not a limitation for ostracods, as several taxa can tolerate extreme salinity variations (for ex., from 6.5 to >30 psu for *Sarsicytheridea bradii*; Stepanova et al., 2019), the turbidity is a more likely

limiting factor. Vertical mixing of the surface waters rich in suspended particulate matter may lead to turbid bottom waters, especially at the shallow site of core HBGC01 (Hill & Nadeau, 1989; Rainville & Woodgate, 2009; see the bottom water masses section). However, turbidity might not be the direct cause. Various physico-chemical effects derived from increased suspended particulate matter supply, like acidification (Semiletov et al., 2016), could also affect ostracod abundance.

CONCLUSIONS

This study presents micropaleontological data of benthic foraminifera, ostracods, and tintinnids that provide time series with annual to multiannual time resolution in an Arctic nearshore environment. The three groups of microfossils provide complementary information on pelagic and bottom water conditions at two sites in the Herschel Basin, one near the summer halocline (HBGC01, 18 m depth) and the other below the halocline (PG2303-1, 32 m depth). The microfaunal communities of the two cores illustrate the sensitivity of micropaleontological tracers to water conditions at local scales, especially with regards to salinity and productivity. The 40-cm-long core HBGC01 covers the period ca. 1969–2018 CE, while a satisfactory age model could not be established for PG2303-1 (20 cm long). A redundancy analysis performed on the foraminiferal assemblages in both cores permitted us to identify ecozones that were also consistent with the ostracod assemblage data and *Tintinnopsis fimbriata* abundance. Thus, the three studied microfossil groups responded simultaneously to decadal environmental changes and can be used as complementary paleo-tracers to distinguish the impacts of recent climate changes over long-scale environmental variations in Arctic nearshore areas.

Among the most important microfaunal changes is an increase in the benthic foraminifera *Eoeponidella pulchella*, which indicates enhanced primary productivity since ~2000 CE. The last two decades are also marked by the high occurrence of the shallow, low-salinity species *Haynesina nivea*, while *Islandiella norcrossi*, which requires more stable saline conditions, decreased in abundance. The microfaunal record of the shallow core HBGC01 thus suggests a transition from stable saline bottom waters to more unstable bottom water salinity. The decrease in summer sea-ice concentration that occurred after 2003 CE and more clearly after 2006 CE might best explain this transition at the basin margin, as the loss in summer sea-ice cover may have led to increased vertical mixing and thus to lower and varying bottom-water salinity. Moreover, the high fluxes of the tintinnid *T. fimbriata* combined with increased sand content, the abundance of *Quinqueloculina stalkeri*, and a reduction in ostracod concentrations during the most recent decade points to enhanced turbidity of the water. Turbid waters could derive from increased inputs of particulate matter-rich freshwaters related to Mackenzie River discharge, local rivers and/or coastal erosion, which could be facilitated in the context of reduced sea-ice cover. We suggest that increased productivity might be caused by enhanced terrigenous organic fluxes and/or upwelling during easterly wind events, which would be amplified under reduced summer sea-ice concentration.

REFERENCES

Agatha, S., 2008, Redescription of the tintinnid ciliate *Tintinnopsis fimbriata* Meunier, 1919 (Spirotricha, Choreotrichida) from coastal waters of Northern Germany: Denisia, v. 23, p. 261–272.

Anthony, K. R., Ridd, P. V., Orpin, A. R., Larcombe, P., and Lough, J., 2004, Temporal variation of light availability in coastal benthic habitats: Effects of clouds, turbidity, and tides: Limnology and Oceanography, v. 49, p. 2201–2211.

Aoyama, M., Hirose, K., and Igarashi, Y., 2006, Re-construction and updating our understanding on the global weapons tests 137Cs fallout: Journal of Environmental Monitoring, v. 8, p. 431–438.

Aquino-López, M. A., Blaauw, M., Christen, J. A., and Sanderson, N. K., 2018, Bayesian analysis of ^{210}Pb dating: Journal of Agricultural, Biological and Environmental Statistics, v. 23, p. 317–333.

Ardyna, M., and Arrigo, K. R., 2020, Phytoplankton dynamics in a changing Arctic Ocean: Nature Climate Change, v. 10, p. 892–903.

Ardyna, M., Babin, M., Devred, E., Forest, A., Gosselin, M., Raimbault, P., and Tremblay, J.-É., 2017, Shelf-basin gradients shape ecological phytoplankton niches and community composition in the coastal Arctic Ocean (Beaufort Sea): Limnology and Oceanography, v. 62, p. 2113–2132.

Arrigo, K. R., and van Dijken, G. L., 2015, Continued increases in Arctic Ocean primary production: Progress in Oceanography, v. 136, p. 60–70.

Arrigo, K. R., van Dijken, G., and Pabi, S., 2008, Impact of a shrinking Arctic ice cover on marine primary production: Geophysical Research Letters, v. 35, DOI: 10.1029/2008GL035028.

Barber, D. G., Asplin, M. G., Papakyriakou, T. N., Miller, L., Else, B. G., Iacozza, J., Mundy, C., Gosslin, M., Asselin, N. C., and Ferguson, S., 2012, Consequences of change and variability in sea ice on marine ecosystem and biogeochemical processes during the 2007–2008 Canadian International Polar Year program: Climatic Change, v. 115, p. 135–159.

Baskaran, M., and Naidu, A. S., 1995, ^{210}Pb-derived chronology and the fluxes of ^{210}Pb and ^{137}Cs isotopes into continental shelf sediments, East Chukchi Sea, Alaskan Arctic: Geochimica et Cosmochimica Acta, v. 59, p. 4435–4448.

Bell, L. E., Bluhm, B. A., and Iken, K., 2016, Influence of terrestrial organic matter in marine food webs of the Beaufort Sea shelf and slope: Marine Ecology Progress Series, v. 550, p. 1–24.

Blais, M., Ardyna, M., Gosselin, M., Dumont, D., Bélanger, S., Tremblay, J.-É., Gratton, Y., Marchese, C., and Poulin, M., 2017, Contrasting interannual changes in phytoplankton productivity and community structure in the coastal Canadian Arctic Ocean: Limnology and Oceanography, v. 62, p. 2480–2497.

Blott, S., 2010, GRADISTAT ver. 8.0: A grain size distribution and statistics package for the analysis of unconsolidated sediments by sieving or laser granulometer: Kenneth Pye Associates, Solihull, UK.

Boetius, A., Grahl, C., Kröncke, I., Liebezeit, G., and Nöthig, E., 1996, Distribution of plant pigments in surface sediments of the Eastern Arctic, in Stein, R., et al. (eds.), Surface-sediment Composition and Sedimentary Processes in the Central Arctic Ocean and Along the Eurasian Continental Margin: Berichte zur Polarforschung 212, Bremerhaven, Alfred Wegener Institute, p. 213–218.

Bonsell, C., and Dunton, K. H., 2018, Long-term patterns of benthic irradiance and kelp production in the central Beaufort Sea reveal implications of warming for Arctic inner shelves: Progress in Oceanography, v. 162, p. 160–170.

Boucsein, B., and Stein, R., 2000, Particulate organic matter in surface sediments of the Laptev Sea (Arctic Ocean): Application of maceral analysis as organic-carbon-source indicator: Marine Geology, v. 162, p. 573–586.

Boyer, T. P., Baranova, O. K., Coleman, C., Garcia, H. E., Grodsky, A., Locarnini, R. A., Mishonov, A.V., Paver C. R., Reagan, J. R., Seidov, D., Smolyar, I. V., Weathers, K., and Zweng, M. M., 2018, World Ocean Database 2018: Mishonov, A.V. Technical Ed., NOAA Atlas NESDIS 87, Retrieved from https://www.ncei.noaa.gov/sites/default/files/2020-04/wod_intro_0.pdf.

Bruel, R., and Sabatier, P., 2020, serac: An R package for ShortlivEd RAdionuclide chronology of recent sediment cores: Journal of Environmental Radioactivity, v. 225, DOI: 10.1016/j.jenvrad.2020.106449.

Brugler, E. T., Pickart, R. S., Moore, G., Roberts, S., Weingartner, T. J., and Statscewich, H., 2014, Seasonal to interannual variability of the Pacific water boundary current in the Beaufort Sea: Progress in Oceanography, v. 127, p. 1–20.

Burkovsky, I., 1976, Ecology of Tintinnida (Ciliata) of the White Sea: Zoologicheskii Zhurnal, v. 55, p. 497–507.

Cage, A. G., Pieńkowski, A. J., Jennings, A., Knudsen, K. L., and Seidenkrantz, M.-S., 2021, Comparative analysis of six common foraminiferal species of the genera Cassidulina, Paracassidulina, and Islandiella from the Arctic–North Atlantic domain: Journal of Micropalaeontology, v. 40, p. 37–60.

Carmack, E. C., and Macdonald, R. W., 2002, Oceanography of the Canadian Shelf of the Beaufort Sea: A setting for marine life: Arctic, v. 55, p. 29–45.

Carmack, E. C., Barber, D., Christensen, J., Macdonald, R., Rudels, B., and Sakshaug, E., 2006, Climate variability and physical forcing of the food webs and the carbon budget on panarctic shelves: Progress in Oceanography, v. 71, p. 145–181.

Carnero-Bravo, V., Falardeau, J., Chassiot, L., Tanski, G., Hillaire-Marcel, C., Ghaleb, B., de Vernal, A., Vonk, J. E., Lantuit, H., Fritz, M., and Preda, M., 2021, Sediment structure and deposition rates in the Yukon coast: PANGAEA, DOI: 10.1594/PANGAEA.937387.

Chernov, I., Lazzari, P., Tolstikov, A., Kravchishina, M., and Iakovlev, N., 2018, Hydrodynamical and biogeochemical spatiotemporal variability in the White Sea: A modeling study: Journal of Marine Systems, v. 187, p. 23–35.

Comeau, A. M., Li, W. K., Tremblay, J.-É., Carmack, E. C., and Lovejoy, C., 2011, Arctic Ocean microbial community structure before and after the 2007 record sea ice minimum: Plos One, v. 6, DOI: 10.1371/journal.pone.0027492.

Corbett, D. R., McKee, B., and Allison, M., 2006, Nature of decadal-scale sediment accumulation on the western shelf of the Mississippi River delta: Continental Shelf Research, v. 26, p. 2125–2140.

Cronin, T. M., Gemery, L., Briggs, W. Jr., Jakobsson, M., Polyak, L., and Brouwers, E., 2010, Quaternary Sea-ice history in the Arctic Ocean based on a new Ostracod sea-ice proxy: Quaternary Science Reviews, v. 29, p. 3415–3429.

Cronin, T. M., O'Regan, M., Pearce, C., Gemery, L., Toomey, M., Semiletov, I., and Jakobsson, M., 2017, Deglacial sea level history of the East Siberian Sea and Chukchi Sea margins: Climate of the Past, v. 13, p. 1097–1110.

Dolan, J., Ritchie, M., and Ras, J., 2007, The "neutral" community structure of planktonic herbivores, tintinnid ciliates of the microzooplankton, across the SE Tropical Pacific Ocean: Biogeosciences, v. 4, p. 297–310.

Dolan, J. R., Yang, E. J., Kim, T. W., and Kang, S.-H., 2014, Microzooplankton in a warming Arctic: A comparison of tintinnids and radiolarians from summer 2011 and 2012 in the Chukchi Sea: Acta Protozoologica, v. 53, p. 101–113.

Doxaran, D., Devred, E., and Babin, M., 2015, A 50% increase in the mass of terrestrial particles delivered by the Mackenzie River into the Beaufort Sea (Canadian Arctic Ocean) over the last 10 years: Biogeosciences, v. 12, p. 3551–3565.

EBA Engineering Consultants Ltd., 1992, Proceedings of the Beaufort Sea granular resources workshop, Part 1: Reports on NOGAP regional studies, 11 p.

Echols, R. J., and Fowler, G. A., 1973, Agglutinated tintinnid loricae from some Recent and Late Pleistocene shelf sediments: Micropaleontology, v. 19, p. 431–443.

Ehn, J. K., Reynolds, R. A., Stramski, D., Doxaran, D., Lansard, B., and Babin, M., 2019, Patterns of suspended particulate matter across the continental margin in the Canadian Beaufort Sea during summer: Biogeosciences, v. 16, p. 1583–1605.

Emmerton, C. A., Lesack, L. F., and Vincent, W. F., 2008, Nutrient and organic matter patterns across the Mackenzie River, estuary and shelf during the seasonal recession of sea-ice: Journal of Marine Systems, v. 74, p. 741–755.

Fatela, F., and Taborda, R., 2002, Confidence limits of species proportions in microfossil assemblages: Marine Micropaleontology, v. 45, p. 169–174.

Feyling-Hanssen, R. W., Jørgensen, J. A., Knudsen, K. L., Lykke-Andersen, A.-L., 1971, Late Quaternary Foraminifera from Vendsyssel, Denmark and Sandnes, Norway: Bulletin of the Geological Society of Denmark, v. 21, p. 67–317.

Feyling-Hanssen, R. W., and Ulleberg, K., 1984, A Tertiary-Quaternary section at Sarsbukta, Spitsbergen, Svalbard, and its foraminifera: Polar Research, v. 2, p. 77–106.

Fortin, D., Francus, P., Gebhardt, A. C., Hahn, A., Kliem, P., Lisé-Pronovost, A., Roychowdhury, R., Labrie, J., and St-Onge, G., The PASADO Science Team, 2013, Destructive and non-destructive density determination: method comparison and evaluation from the Laguna Potrok Aike sedimentary record: Quaternary Science Reviews, v. 71, p. 147–153.

Frey, K. E., Moore, G., Cooper, L. W., and Grebmeier, J. M., 2015, Divergent patterns of recent sea ice cover across the Bering, Chukchi, and Beaufort seas of the Pacific Arctic Region: Progress in Oceanography, v. 136, p. 32–49.

Fritz, M., Vonk, J. E., and Lantuit, H., 2017, Collapsing Arctic coastlines: Nature Climate Change, v. 7, p. 6–7.

Fütterer, D., 1994, Die Expedition ARCTIC'93: der Fahrtabschnitt ARK-IX/4 mit FS "Polarstern" 1993: Berichte zur Polarforschung 149, Bremerhaven, Alfred Wegener Institute, 244 p.

Gemery, L., Cronin, T., Cooper, L., and Grebmeier, J., 2013, Temporal changes in benthic ostracod assemblages in the Northern Bering

and Chukchi Seas from 1976 to 2010: Deep Sea Research Part II: Topical Studies in Oceanography, v. 94, p. 68–79.

Gemery, L., Cronin, T. M., Briggs, W. M., Brouwers, E. M., Schornikov, E. I., Stepanova, A., Wood, A. M., and Yasuhara, M., 2017, An Arctic and Subarctic ostracod database: Biogeographic and paleoceanographic applications: Hydrobiologia, v. 786, p. 59–95.

Gemery, L., Cronin, T. M., Cooper, L. W., Dowsett, H. J., and Grebmeier, J. M., 2021, Biogeography and ecology of Ostracoda in the US northern Bering, Chukchi, and Beaufort Seas: Plos One, v. 16, DOI: 10.1371/journal.pone.0251164.

Environment and Climate Change Canada, Historical Hydrometric Data, Retrieved April, 2020 from https://wateroffice.ec.gc.ca/mainmenu/historical_data_index_e.html.

Grebmeier, J. M., Cooper, L. W., Feder, H. M., and Sirenko, B. I., 2006, Ecosystem dynamics of the Pacific-influenced northern Bering and Chukchi Seas in the Amerasian Arctic: Progress in Oceanography, v. 71, p. 331–361.

Griffiths, J., 2010, Microfossil Evidence for Recent and Past Changes to Hudson Bay Oceanography: Dalhousie University, Halifax, 115 p.

Grotheer, H., Meyer, V., Riedel, T., Pfalz, G., Mathieu, L., Hefter, J., Gentz, T., Lantuit, H., Mollenhauer, G., and Fritz, M., 2020, Burial and origin of permafrost-derived carbon in the nearshore zone of the southern Canadian Beaufort Sea: Geophysical Research Letters, v. 47, DOI: 10.1029/2019GL085897.

Guilbault, J.-P., Barrie, J.V., Conway, K., Lapointe, M., and Radi, T., 2003, Paleoenvironments of the Strait of Georgia, British Columbia during the last deglaciation: Microfaunal and microfloral evidence: Quaternary Science Reviews, v. 22, p. 839–857.

Günther, F., Overduin, P. P., Yakshina, I. A., Opel, T., Baranskaya, A. V., and Grigoriev, M. N., 2015, Observing Muostakh disappear: Permafrost thaw subsidence and erosion of a ground-ice-rich island in response to arctic summer warming and sea ice reduction: The Cryosphere, v. 9, p. 151–178.

Hald, M., and Korsun, S., 1997, Distribution of modern benthic foraminifera from fjords of Svalbard, European Arctic: Journal of Foraminiferal Research, v. 27, p. 101–122.

Hald, M., and Steinsund, P., 1996, Benthic foraminifera and carbonate dissolution in the surface sediments of the Barents and Kara Sea *in* Stein, R., et al. (eds.), Surface-sediment Composition and Sedimentary Processes in the Central Arctic Ocean and Along the Eurasian Continental Margin: Berichte zur Polarforschung 212, Bremerhaven, Alfred Wegener Institute, p. 285–307.

Hanna, A. J., Allison, M. A., Bianchi, T. S., Marcantonio, F., and Goff, J. A., 2014, Late Holocene sedimentation in a high Arctic coastal setting: Simpson Lagoon and Colville Delta, Alaska: Continental Shelf Research, v. 74, p. 11–24.

Hansen, A., and Knudsen, K. L., 1995, Recent foraminiferal distribution in Freemansundet and Early Holocene stratigraphy on Edgeøya, Svalbard: Polar Research, v. 14, p. 215–238.

Hill, P. R., and Nadeau, O. C., 1989, Storm-dominated sedimentation on the inner shelf of the Canadian Beaufort Sea: Journal of Sedimentary Research, v. 59, p. 455–468.

Holmes, R. M., McClelland, J. W., Peterson, B. J., Tank, S. E., Bulygina, E., Eglinton, T. I., Gordeev, V. V., Gurtovaya, T. Y., Raymond, P. A., and Repeta, D. J., 2011, Seasonal and annual fluxes of nutrients and organic matter from large rivers to the Arctic Ocean and surrounding seas: Estuaries and Coasts, v. 35, p. 369–382.

Husum, K., Hald, M., Stein, R., and Weißschnur, M., 2015, Recent benthic foraminifera in the Arctic Ocean and Kara Sea continental margin: Arktos, v. 1, DOI: 10.1007/s41063-015-0005-9.

IPCC, 2019, IPCC Special Report on the Ocean and Cryosphere in a Changing Climate: Cambridge University Press, Cambridge, 755 p.

Itaki, T., Ito, M., Narita, H., Ahagon, N., and Sakai, H., 2003, Depth distribution of radiolarians from the Chukchi and Beaufort Seas, western Arctic: Deep Sea Research Part I: Oceanographic Research Papers, v. 50, p. 1507–1522.

Janout, M. A., Aksenov, Y., Hölemann, J. A., Rabe, B., Schauer, U., Polyakov, I. V., Bacon, S., Coward, A. C., Karcher, M., and Lenn, Y. D., 2015, Kara Sea freshwater transport through Vilkitsky Strait: Variability, forcing, and further pathways toward the western Arctic Ocean from a model and observations: Journal of Geophysical Research: Oceans, v. 120, p. 4925–4944.

Jennings, A., Andrews, J., Reilly, B., Walczak, M., Jakobsson, M., Mix, A., Stoner, J., Nicholls, K. W., and Cheseby, M., 2020, Modern foraminiferal assemblages in northern Nares Strait, Petermann Fjord, and beneath Petermann ice tongue, NW Greenland: Arctic, Antarctic, and Alpine Research, v. 52, p. 491–511.

Jones, B. M., Arp, C. D., Jorgenson, M. T., Hinkel, K. M., Schmutz, J. A., and Flint, P. L., 2009, Increase in the rate and uniformity of coastline erosion in Arctic Alaska: Geophysical Research Letters, v. 36, DOI: 10.1029/2008GL036205.

Jong, D., Bröder, L., Tanski, G., Fritz, M., Lantuit, H., Tesi, T., Haghipour, N., Eglinton, T. I., and Vonk, J. E., 2020, Nearshore zone dynamics determine pathway of organic carbon from eroding permafrost coasts: Geophysical Research Letters, v. 47, DOI: 10.1029/2020GL088561.

Juhls, B., 2021, Land-Ocean Interactions in Arctic Coastal Waters: Ocean Colour Remote Sensing and Current Carbon Fluxes to the Arctic Ocean: Freie Universität Berlin, Berlin, 165 p.

Kinnard, C., Zdanowicz, C. M., Fisher, D. A., Isaksson, E., de Vernal, A., and Thompson, L. G., 2011, Reconstructed changes in Arctic sea ice over the past 1,450 years: Nature, v. 479, p. 509–512.

Klein, K. P., Lantuit, H., Heim, B., Fell, F., Doxaran, D., and Irrgang, A. M., 2019, Long-term high-resolution sediment and sea surface temperature spatial patterns in Arctic nearshore waters retrieved using 30-year landsat archive imagery: Remote Sensing, v. 11, DOI: 10.3390/rs11232791.

Knudsen, K. L., Stabell, B., Seidankrantz, M.-S., Eiriksson, J., and Blake, W., Jr., 2008, Deglacial and Holocene conditions in northernmost Baffin Bay: Sediments, foraminifera, diatoms and stable isotopes: Boreas, v. 37, p. 346–376.

Kulikov, E., Carmack, E. C., and Macdonald, R., 1998, Flow variability at the continental shelf break of the Mackenzie Shelf in the Beaufort Sea: Journal of Geophysical Research: Oceans, v. 103, p. 12725–12741.

Kutos, O., Rochon, A., and Montero-Serrano, J.-C., 2021, Evolution of palaeo-sea-surface conditions and sediment dynamics over the last 2700 years on the Mackenzie Slope, Beaufort Sea (Canadian Arctic): Boreas, v. 50, p. 893–914.

Lefebvre, K. A., Quakenbush, L., Frame, E., Huntington, K. B., Sheffield, G., Stimmelmayr, R., Bryan, A., Kendrick, P., Ziel, H., and Goldstein, T., 2016, Prevalence of algal toxins in Alaskan marine mammals foraging in a changing arctic and subarctic environment: Harmful Algae, v. 55, p. 13–24.

Lewis, K., Van Dijken, G., and Arrigo, K. R., 2020, Changes in phytoplankton concentration now drive increased Arctic Ocean primary production: Science, v. 369, p. 198–202.

Li, W. K., 2014, The state of phytoplankton and bacterioplankton at the Compass Buoy Station: Bedford Basin monitoring program 1992–2013: Fisheries and Oceans Canada Pêches et Océans Canada, 138 p.

Li, W. K., McLaughlin, F. A., Lovejoy, C., and Carmack, E. C., 2009, Smallest algae thrive as the Arctic Ocean freshens: Science, v. 326, p. 539.

Lin, P., Pickart, R. S., Stafford, K. M., Moore, G., Torres, D. J., Bahr, F., and Hu, J., 2016, Seasonal variation of the Beaufort shelfbreak jet and its relationship to Arctic cetacean occurrence: Journal of Geophysical Research: Oceans, v. 121, p. 8434–8454.

Lin, P., Pickart, R. S., Fissel, D., Ross, E., Kasper, J., Bahr, F., Torres, D. J., O'Brien, J., Borg, K., and Melling, H., 2020, Circulation in the vicinity of Mackenzie Canyon from a year-long mooring array: Progress in Oceanography, v. 187, DOI: 10.1016/j.pocean.2020.102396.

Lloyd, J. M., 2006, Modern distribution of benthic foraminifera from Disko Bugt, West Greenland: Journal of Foraminiferal Research, v. 36, p. 315–331.

Luoto, T. P., Nevalainen, L., Kubischta, F., Kultti, S., Knudsen, K. L., and Salonen, V. P., 2011, Late quaternary ecological turnover in high arctic Lake Einstaken, Nordaustlandet, Svalbard (80 N). Geografiska Annaler: Series A: Physical Geography, v. 93, p. 337–354.

Madsen, H. B., and Knudsen, K. L., 1994, Recent foraminifera in shelf sediments of the Scoresby Sund fjord, East Greenland: Boreas, v. 23, p. 495–504.

McDougall, K. A., Brouwers, E. M., and Smith, P., 1986, Micropaleontology and sedimentology of the PB borehole series, Prudhoe

Bay, Alaska: U.S. Geological Survey Bulletin 1598, 62 p., DOI: 10.3133/b1598.

McLaughlin, F. A., and Carmack, E. C., 2010, Deepening of the nutricline and chlorophyll maximum in the Canada Basin interior, 2003–2009: Geophysical Research Letters, v. 37, DOI: 10.1029/2010GL045459.

Meier, W. N., Fetterer, F., Savoie, M., Mallory, S., Duerr, R., and Stroeve, J., 2017, NOAA/NSIDC Climate Data Record of Passive Microwave Sea Ice Concentration, Version 3. [goddard_merged_seaice_conc]. Boulder, Colorado USA. NSIDC: National Snow and Ice Data Center. [January 2020].

Meunier, A., 1919, Mikroplankton de la mer Flamande. III. Les Péridiniens: Mémoires du Musée Royal d'Histoire Naturelle de Belgique, v. 8, p. 1–116.

Mioduszewski, J., Vavrus, S., and Wang, M., 2018, Diminishing Arctic sea ice promotes stronger surface winds: Journal of Climate, v. 31, p. 8101–8119.

Moffitt, S. E., Hill, T. M., Ohkushi, K., Kennett, J. P., and Behl, R. J., 2014, Vertical oxygen minimum zone oscillations since 20 ka in Santa Barbara Basin: A benthic foraminiferal community perspective: Paleoceanography, v. 29, p. 44–57.

Nürnberg, D., 1996, Biogenic barium and opal in shallow Eurasian shelf sediments in relation to the pelagic Arctic Ocean environment, in Stein, R., et al. (eds.), Surface-sediment Composition and Sedimentary Processes in the Central Arctic Ocean and Along the Eurasian Continental Margin: Berichte zur Polarforschung 112, Bremerhaven, Alfred Wegener Institute, p. 96–118.

Obu, J., Lantuit, H., Fritz, M., Pollard, W. H., Sachs, T., and Günther, F., 2016, Relation between planimetric and volumetric measurements of permafrost coast erosion: A case study from Herschel Island, western Canadian Arctic: Polar Research, v. 35, DOI: 10.3402/polar.v35.30313.

Ogi, M., and Wallace, J. M., 2007, Summer minimum Arctic sea ice extent and the associated summer atmospheric circulation: Geophysical Research Letters, v. 34, DOI: 10.1029/2007GL029897.

Ogi, M., Rigor, I. G., McPhee, M. G., and Wallace, J. M., 2008, Summer retreat of Arctic sea ice: Role of summer winds: Geophysical Research Letters, v. 35, DOI: 10.1029/2008GL035672.

Oksanen, J., Blanchet, F. G., Kindt, R., Legendre, P., Minchin, P. R., O'Hara, R., Simpson, G. L., Solymos, P., Stevens, M. H. H., and Wagner, H., 2013, Package 'vegan', Community Ecology Package, version 2, 295 p.

Olausson, E., 1982, The Pleistocene/Holocene boundary in southwestern Sweden: Sveriges Geologiska Undersökning. Ser. C, v. 794, 288 p.

Osadchiev, A., Silvestrova, K., and Myslenkov, S., 2020, Wind-driven coastal upwelling near large river deltas in the Laptev and east-Siberian seas: Remote Sensing, v. 12, DOI: 10.3390/rs12050844.

Overeem, I., Anderson, R. S., Wobus, C. W., Clow, G. D., Urban, F. E., and Matell, N., 2011, Sea ice loss enhances wave action at the Arctic coast: Geophysical Research Letters, v. 38, DOI: 10.1029/2011GL048681.

Paranjape, M. A., 1987, The seasonal cycles and vertical distribution of tintinnines in Bedford Basin, Nova Scotia, Canada: Canadian Journal of Zoology, v. 65, p. 41–48.

Pfalz, G., 2017, Lateral transport of sediment and organic matter, derived from coastal erosion, into the nearshore zone of the southern Beaufort Sea, Canada: Technische Universität Dresden, Dresden, 66 p.

Pickart, R. S., 2004, Shelfbreak circulation in the Alaskan Beaufort Sea: Mean structure and variability: Journal of Geophysical Research: Oceans, v. 109, DOI: 10.1029/2003JC001912.

Pickart, R. S., Spall, M. A., Moore, G. W., Weingartner, T. J., Woodgate, R. A., Aagaard, K., and Shimada, K., 2011, Upwelling in the Alaskan Beaufort Sea: Atmospheric forcing and local versus non-local response: Progress in Oceanography, v. 88, p. 78–100.

Pickart, R. S., Spall, M. A., and Mathis, J. T., 2013, Dynamics of upwelling in the Alaskan Beaufort Sea and associated shelf–basin fluxes: Deep Sea Research Part I: Oceanographic Research Papers, v. 76, p. 35–51.

Pierce, R. W., and Turner, J. T., 1993, Global biogeography of marine tintinnids: Marine Ecology Progress Series, v. 94, p. 11–26.

Poag, C. W., and Tresslar, R. C., 1981, Living foraminifers of West Flower Garden Bank, northernmost coral reef in the Gulf of Mexico: Micropaleontology, v. 27, p. 31–62.

Polyak, L., Korsun, S., Febo, L. A., Stanovoy, V., Khusid, T., Hald, M., Paulsen, B. E., and Lubinski, D. J., 2002, Benthic foraminiferal assemblages from the southern Kara Sea, a river-influenced Arctic marine environment: Journal of Foraminiferal Research, v. 32, p. 252–273.

Polyak, L., Stanovoy, V., and Lubinski, D. J., 2003, Stable isotopes in benthic foraminiferal calcite from a river-influenced Arctic marine environment, Kara and Pechora Seas: Paleoceanography, v. 18, DOI: 10.1029/2001PA000752.

R Core Team, 2021, R: A language and environment for statistical computing. R Foundation for Statistical Computing, Vienna, Austria, Retrieved from https://www.R-project.org/.

Radosavljevic, B., Lantuit, H., Pollard, W., Overduin, P., Couture, N., Sachs, T., Helm, V., and Fritz, M., 2016, Erosion and flooding—threats to coastal infrastructure in the Arctic: A case study from Herschel Island, Yukon Territory, Canada: Estuaries and Coasts, v. 39, p. 900–915.

Rainville, L., and Woodgate, R. A., 2009, Observations of internal wave generation in the seasonally ice-free Arctic: Geophysical Research Letters, v. 36, DOI: 10.1029/2009GL041291.

Rasband, W. S., 1997–2018, ImageJ, U. S. National Institutes of Health, Bethesda, Maryland, USA, https://imagej.nih.gov/ij/.

Reimnitz, E., McCormick, M., McDougall, K., and Brouwers, E., 1993, Sediment export by ice rafting from a coastal polynya, Arctic Alaska, USA: Arctic and Alpine Research, v. 25, p. 83–98.

Retamal, L., Bonilla, S., and Vincent, W. F., 2008, Optical gradients and phytoplankton production in the Mackenzie River and the coastal Beaufort Sea: Polar Biology, v. 31, p. 363–379.

Rogers, G., Roff, J., and Lynn, D., 1981, Tintinnids of Chesterfield Inlet, Northwest Territories: Canadian Journal of Zoology, v. 59, p. 2360–2364.

Sanchez-Cabeza, J., and Ruiz-Fernández, A., 2012, 210Pb sediment radiochronology: An integrated formulation and classification of dating models: Geochimica et Cosmochimica Acta, v. 82, p. 183–200.

Schlitzer, R., 2018, Ocean Data View, Alfred Wegener Institute, https://odv.awi.de.

Schulze, L. M., and Pickart, R. S., 2012, Seasonal variation of upwelling in the Alaskan Beaufort Sea: Impact of sea ice cover: Journal of Geophysical Research: Oceans, v. 117, DOI: 10.1029/2012JC007985.

Scott, D. B., Schell, T., Rochon, A., and Blasco, S., 2008a, Benthic foraminifera in the surface sediments of the Beaufort Shelf and slope, Beaufort Sea, Canada: Applications and implications for past sea-ice conditions: Journal of Marine Systems, v. 74, p. 840–863.

Scott, D. B., Schell, T., Rochon, A., and Blasco, S., 2008b, Modern benthic foraminifera in the surface sediments of the Beaufort Shelf, Slope and Mackenzie Trough, Beaufort Sea, Canada: Taxonomy and summary of surficial distributions: Journal of Foraminiferal Research, v. 38, p. 228–250.

Seidenkrantz, M.-S., 2013, Benthic foraminifera as palaeo sea-ice indicators in the subarctic realm–examples from the Labrador Sea–Baffin Bay region: Quaternary Science Reviews, v. 79, p. 135–144.

Seidenstein, J. L., Cronin, T. M., Gemery, L., Keigwin, L. D., Pearce, C., Jakobsson, M., Coxall, H. K., Wei, E. A., and Driscoll, N. W., 2018, Late Holocene paleoceanography in the Chukchi and Beaufort Seas, Arctic Ocean, based on benthic foraminifera and ostracods: Arktos, v. 4, DOI: 10.1007/s41063-018-0058-7.

Semiletov, I., Pipko, I., Gustafsson, Ö., Anderson, L. G., Sergienko, V., Pugach, S., Dudarev, O., Charkin, A., Gukov, A., and Bröder, L., 2016, Acidification of East Siberian Arctic Shelf waters through addition of freshwater and terrestrial carbon: Nature Geoscience, v. 9, p. 361–365.

Serreze, M. C., and Barrett, A. P., 2011, Characteristics of the Beaufort Sea high: Journal of Climate, v. 24, p. 159–182.

Sherr, E. B., Sherr, B. F., and Hartz, A. J., 2009, Microzooplankton grazing impact in the Western Arctic Ocean: Deep Sea Research Part II: Topical Studies in Oceanography, v. 56, p. 1264–1273.

Simmonds, I., and Keay, K., 2009, Extraordinary September Arctic sea ice reductions and their relationships with storm

behavior over 1979–2008: Geophysical Research Letters, v. 36, DOI: 10.1029/2009GL039810.

Smith, D. C., and Morison, J. H., 1998, Nonhydrostatic haline convection under leads in sea ice: Journal of Geophysical Research: Oceans, v. 103, p. 3233–3247.

Souto, S., 1973, Contribución al conocimiento de los tintínnidos de agua dulce de la República Argentina. I Río de la Plata y Delta del Paraná: Physis, v. 32, p. 249–254.

Stepanova, A., Taldenkova, E., and Bauch, H. A., 2003, Recent Ostracoda from the Laptev Sea (Arctic Siberia): Species assemblages and some environmental relationships: Marine Micropaleontology, v. 48, p. 23–48.

Stepanova, A., Taldenkova, E., Simstich, J., and Bauch, H. A., 2007, Comparison study of the modern ostracod associations in the Kara and Laptev seas: Ecological aspects: Marine Micropaleontology, v. 63, p. 111–142.

Stepanova, A., Obrochta, S., Quintana Krupinski, N. B., Hyttinen, O., Kotilainen, A., and Andrén, T., 2019, Late Weichselian to Holocene history of the Baltic Sea as reflected in ostracod assemblages: Boreas, v. 48, p. 761–778.

Terhaar, J., Lauerwald, R., Regnier, P., Gruber, N., and Bopp, L., 2021, Around one third of current Arctic Ocean primary production sustained by rivers and coastal erosion: Nature Communications, v. 12, DOI: 10.1038/s41467-020-20470-z.

Tian, S. Y., Yasuhara, M., Hong, Y., Huang, H.-H. M., Iwatani, H., Chiu, W.-T. R., Mamo, B., Okahashi, H., and Rasmussen, T. L., 2020, Deglacial–Holocene Svalbard paleoceanography and evidence of meltwater pulse 1B: Quaternary Science Reviews, v. 233, DOI: 10.1016/j.quascirev.2020.106237.

Tremblay, J.-É., Bélanger, S., Barber, D., Asplin, M., Martin, J., Darnis, G., Fortier, L., Gratton, Y., Link, H., and Archambault, P., 2011, Climate forcing multiplies biological productivity in the coastal Arctic Ocean: Geophysical Research Letters, v. 38, DOI: 10.1029/2011GL048825.

Tremblay, J.-É., Robert, D., Varela, D. E., Lovejoy, C., Darnis, G., Nelson, R. J., and Sastri, A. R., 2012, Current state and trends in Canadian Arctic marine ecosystems: I. Primary production: Climatic Change, v. 115, p. 161–178.

Tremblay, J.-É., Raimbault, P., Garcia, N., Lansard, B., Babin, M., and Gagnon, J., 2014, Impact of river discharge, upwelling and vertical mixing on the nutrient loading and productivity of the Canadian Beaufort Shelf: Biogeosciences, v. 11, p. 4853–4868.

Voltski, I., Korsun, S., Pillet, L., and Pawlowski, J., 2015, *Protoelphidium niveum* and the taxonomy of "lower" elphidiids: Journal of Foraminiferal Research, v. 45, p. 250–263.

Walkusz, W., Williams, W. J., Harwood, L. A., Moore, S. E., Stewart, B. E., and Kwasniewski, S., 2012, Composition, biomass and energetic content of biota in the vicinity of feeding bowhead whales (*Balaena mysticetus*) in the Cape Bathurst upwelling region (south eastern Beaufort Sea): Deep Sea Research Part I: Oceanographic Research Papers, v. 69, p. 25–35.

Weingartner, T. J., Danielson, S. L., Potter, R. A., Trefry, J. H., Mahoney, A., Savoie, M., Irvine, C., and Sousa, L., 2017, Circulation and water properties in the landfast ice zone of the Alaskan Beaufort Sea: Continental Shelf Research, v. 148, p. 185–198.

Whatley, R. C., 1983, The application of Ostracoda to palaeoenvironmental analysis, *in* Maddocks, R. F. (ed.), Applications of Ostracoda: University of Houston, Geoscience, Houston, p. 51–77.

Williams, B., and Carmack, E. C., 2012, Ocean water and sea ice, *in* Burn, C. R. (ed.), Herschel Island Qikiqtaryuk: A Natural and Cultural History of Yukon's Arctic Island, University of Calgary Press, Calgary, p. 54–59.

Williams, W. J., and Carmack, E. C., 2015, The "interior" shelves of the Arctic Ocean: Physical oceanographic setting, climatology and effects of sea-ice retreat on cross-shelf exchange: Progress in Oceanography, v. 139, p. 24–41.

Wollenburg, J. E., and Kuhnt, W., 2000, The response of benthic foraminifers to carbon flux and primary production in the Arctic Ocean: Marine Micropaleontology, v. 40, p. 189–231.

Wollenburg, J. E., and Mackensen, A., 1998, Living benthic foraminifers from the central Arctic Ocean: Faunal composition, standing stock and diversity: Marine Micropaleontology, v. 34, p. 153–185.

Wood, K. R., Bond, N. A., Danielson, S. L., Overland, J. E., Salo, S. A., Stabeno, P. J., and Whitefield, J., 2015, A decade of environmental change in the Pacific Arctic region: Progress in Oceanography, v. 136, p. 12–31.

Cushman
Foundation for
Foraminiferal
Research

Est. 1950